SVEUČILIŠTE U SPLITU
FAKULTET ELEKTROTEHNIKE, STROJARSTVA I BRODOGRADNJE

POSLIJEDIPLOMSKI DOKTORSKI STUDIJ ELEKTROTEHNIKE I INFORMACIJSKIH TEHNOLOGIJA

KVALIFIKACIJSKI ISPIT

MJERENJE KOMPLEKSNE DIELEKTRIČNE PERMITIVNOSTI U MIKROVALNOM PODRUČJU KOAKSIJALNOM SONDOM OTVORENOG KRAJA

Anđela Matković

Split, ožujak 2022.

UNIVERSITY OF SPLIT
FACULTY OF ELECTRICAL ENGINEERING, MECHANICAL ENGINEERING AND NAVAL ARCHITECTURE

POSTGRADUATE DOCTORAL STUDY OF ELECTRICAL ENGINEERING AND INFORMATION TECHNOLOGY

QUALIFYING EXAM

MEASUREMENT OF THE COMPLEX DIELECTRIC PERMITTIVITY IN THE MICROWAVE RANGE USING AN OPEN-ENDED COAXIAL PROBE

Anđela Matković

Split, March 2022

CONTENTS

1. Introduction

Frequency dependent complex dielectric permittivity is one of the fundamental electromagnetic properties of materials. Although its use in electrical engineering is commonly associated with designing dielectrics used in capacitors or coaxial cables, dielectric permittivity determination has many other, arguably more exciting applications in terms of material sensing. Complex dielectric permittivity of a material varies with temperature [1], moisture content [2], pH value [3], pressure [4], etc. so it is clear that it can give valuable information about the state of a material. It can help discern between e.g. fresh and spoiled foods [5], materials compositions in construction industry, diverse soil compositions [6], healthy and damaged tissue [7], and much more.

Measurement and subsequent calculation of the complex dielectric permittivity can be carried out by a variety of different methods. The choice of suitable method depends on the sample size and type, frequency range, desired accuracy, and other measurement conditions. Dielectric measurements in the microwave frequency range include various reflection, resonant, and combined reflection and transmission methods. One of the most widely used reflection methods is based on the open-ended coaxial probe (OECP) as the dielectric sensor. This method is non-destructive and non-invasive, while at the same time convenient and suitable for wideband measurements in the microwave frequency range. These important features, along with its ease of use and overall stable performance, increased its popularity and expanded its use, which adds to the rationale for this state-of-the-art review to focus on the of the open-ended coaxial probe (OECP) as the method of choice.

OECP method has established itself in the food industry as a reliable system of inspecting food. Mostly, it is used to nondestructively determine the content and quality of various foods. Some examples include determining the water content in oil palm fruits [2], apples [8], macadamia nut kernels [9], sugar content in watermelon juice [10], quality of apples [11], mangoes [12], honey purity [13], evaluation of meat [14] and egg [15] ageing, controlling the meat salting process [16], and many more. Its low cost implementation made it useful for starch content estimation of cassava roots which is a primary food staple in sub-Saharan Africa as the only available alternative was an expensive qualitative laboratory analysis [17]. It is also precise enough to help better monitoring of delicate food production processes to optimize the quality of the finished product as detailed in Carasau bread dough example in [18].

Other industries have also found relevant areas for the application of permittivity measurements done with coaxial probes to improve the overall procedures. Construction industry is interested in obtaining the best mechanical properties from the materials which often includes mixing of different constituents into the material. For instance, the authors in [19] wanted to nondestructively measure the steel fiber content in the concrete as it defines the strength of the material. The OECP method provided them with a quick and easy way of predicting the properties of the bulk material without knowing the original mixing ratio. It can also help to determine the health of a material as the corrosion level is difficult to detect without the destruction of the integrity of the concrete. As the authors [20] in noted, higher corrosion level lowers the dielectric constant and loss factor, which enables the estimation of the rust level based on the permittivity measurements. It has even found its spot in the petroleum industry where it is used for the detection of unwanted sand grains in produced petroleum fluids that cause erosion of the fluid transport and processing equipment [21]. On the other hand, in pharmaceutical industry it is essential to have a controlled moisture content of a pharmaceutical powder during the whole mixing process. Gradinarsky *et al.* [22] have acknowledged that the OECP is a suitable choices for moisture control as its results are independent on the mixing impeller speed used to powder the ingredients.

Soil contamination can also be easily identified with the OECP as shown in [23] which can then be used for soil monitoring and management for agricultural production. In general, measurements of different classes of soils at different moisture contents proved adequate for further analysis of penetration depth of electromagnetic field in the soil as demonstrated in [24]. Knowing the permittivity of the soil is also required for disinfection of the soil by microwave heating. Authors in [25] compared peat, loam, and sand permittivity properties using OECP to better understand the best heating procedure for each soil.

OECP is commonly used to measure the dielectric permittivity of various biological tissues, both in vivo and ex vivo on the excised tissues. The obtained values serve as the reference values in various biomedical applications, e.g., electromagnetic hyperthermia and ablation planning [26], microwave imaging [27], [28], etc. One of the easiest OECP implementations is the analysis of the skin permittivity as the probe is used on the skin surface. OECP measurements are sensitive enough to discern different burn depths of the tissue without the destruction of the sample [7].

Overall, it is indisputable that the open-ended coaxial probe allows for a variety of different applications because of its flexibility and ease of use. Since it is also a broadband method, it can be implemented both using larger probes at lower frequencies for bulk sampling, or all the way up to tens of gigahertz where the probe sizes are significantly smaller and allow for minute samples. As the permittivity of a material is interconnected with various other material properties, there is a potential for even greater and wider application of the method. As a result, this method has been analyzed in literature and research progress has been made in various aspects, but there is still the potential for significant advancements by overcoming the existing limitations of its practical use, as will be shown by this review of the state of the art.

A general introduction into dielectric properties of materials will be presented in Chapter 2. An outline of some of the most popular dielectric measurement methods in the microwave frequency range will be given in Chapter 3. Chapter 4 will present the OECP method and the underlying physics of it, including the calibration method and common de-embedding models that convert the measured complex reflection coefficient into dielectric permittivity. Depending on the measured material properties and the probe physical characteristics, different de-embedding methods will give results with varying accuracy. Chapter 5 is dedicated to the common issues that arise during measurements with the OECP and cover the current research done to overcome such limitations. Issues are apparent when examining the formal measurement restrictions and guidelines of commercial OECP measurement setups. Material under test (MUT) is generally assumed to be homogeneous, with excellent contact with the probe without any gaps, and seemingly infinite in size. As it is not always possible to satisfy those requirements in the real-life measurements, further research is needed to better understand the scope of the limitations to utilize the technique on an even larger scale in the future applications.

2. Dielectric permittivity of materials

Every material is characterized by certain physical properties, which can be expressed using measurable quantities that help describe the material and allow comparison between different materials. All material properties are dependent on the material microscopic and macroscopic states. Additionally, different properties of the same material are frequently related to one another which allows for calculation of some properties from others. This work will focus solely on the macroscopic electromagnetic properties of materials. Electromagnetic properties of a material determine its response to electric and magnetic fields, as well as how electromagnetic fields (EMFs) penetrate and propagate through a given material. The interaction between material and EMFs can be described by Maxwell's equations proposed in 1864:

$$\nabla \cdot \vec{D} = \rho \,, \tag{2.1}$$

$$\nabla \cdot \vec{B} = 0 \,, \tag{2.2}$$

$$\nabla \times \vec{E} = -\frac{\partial \vec{B}}{\partial t} \,, \tag{2.3}$$

$$\nabla \times \vec{H} = \vec{J} + \frac{\partial \vec{D}}{\partial t}. \tag{2.4}$$

They are complemented with the following constitutive relations:

$$\vec{D} = \epsilon \vec{E}, \tag{2.5}$$

$$\vec{B} = \mu \vec{H} \,, \tag{2.6}$$

$$\vec{J} = \sigma \vec{E} \,, \tag{2.7}$$

where:

$\vec{D}$ is the dielectric displacement vector,
ρ is the charge density,
$\vec{B}$ is the magnetic flux density vector,
$\vec{E}$ is the electric field vector,
$\vec{H}$ is the magnetic field vector,
$\vec{J}$ is the current density vector,
ϵ is the complex permittivity of the media,
μ is the complex permeability of the media,
σ is the conductivity of the media.

When a conductor is put into external electric field, charges in it flow through the material. On the contrary, when a dielectric material is put into external electric field, charges just shift from their average equilibrium positions, creating dipoles with their axes aligned with the field lines, resulting in dielectric polarization. Dipoles create an internal electric field in the material in the

opposite direction of the external field which reduces the total field within it. For a pure dielectric material, the polarization, or a dipole moment per unit volume, is defined as:

$$\vec{P} = \epsilon_0 \chi_e \vec{E} \tag{2.8}$$

where:

ϵ_0 equals 8.8541878128 x 10^{-12} F/m and is the permittivity of vacuum and

χ_e is the dielectric susceptibility and equals $\epsilon_r - 1$.

Complex dielectric permittivity ϵ of a material describes the ability of that material to be polarized by external electric field. The greater the magnitude of the complex dielectric permittivity, the higher the polarizability of a material. A more commonly used parameter is the relative permittivity:

$$\epsilon_r = \frac{\epsilon}{\epsilon_0} \tag{2.9}$$

which represents the dimensionless dielectric permittivity because it is normalized to the permittivity of the vacuum. The relative permittivity is a complex number and can be specified as:

$$\epsilon_r = \epsilon_r' - i\epsilon_r''. \tag{2.10}$$

The real part of the relative permittivity ϵ_r' is a measure of the stored energy from an external electric field, while ϵ_r'' is a measure of the loss of energy and is therefore also called loss factor. Complex permittivity can be drawn in a complex plane where its real and imaginary components are drawn with 90° shift as shown in Figure 2.1. The angle δ is formed between total complex permittivity and positive portion of real axis. Consequently,

$$\tan(\delta) = \frac{\epsilon_r''}{\epsilon_r'} \tag{2.11}$$

expresses a ratio of energy lost to the energy stored. This ratio is also known as **loss tangent**.

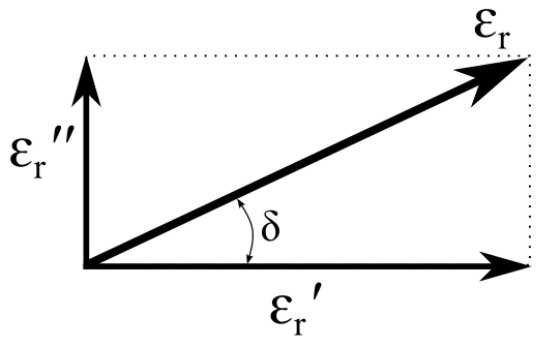

Figure 2.1. Complex permittivity.

The common way to display complex permittivity is to plot real and imaginary parts as a function of frequency on two separate plots. However, since the electric conductivity σ is linked with the imaginary part of relative permittivity through $\sigma = \omega\epsilon_r$", it is not uncommon to see plots of real part of relative permittivity and conductivity.

Dielectric dispersion is the dependence of the complex permittivity of a dielectric material on the frequency of an applied electric field. The exact values of permittivity are dependent on the dielectric mechanisms such as ionic, dipolar, atomic, and electronic polarization, with each mechanism having its associated frequency spectrum as shown in the Figure 2.2. There are no sharp cutoff frequencies for the dielectric mechanisms as their contribution overlaps, but there are observable resonance effects as depicted for the atomic and electronic polarizations. Ionic polarization happens at lower frequencies when the electric field displaces ions in the sublattices of ionic crystals such as NaCl. Dipolar relaxation takes effect in molecules where the shared electrons create a charge imbalance and create a permanent dipole moment. Without the external electric field, the dipole moments are randomly oriented and thus the total polarization is zero. Under the electric field the total polarization will be non-zero. Dipolar polarization is sometimes referred to as orientational polarization. Atomic polarization occurs at higher frequencies because of the shift in the mean positions of atomic nuclei within the molecules or lattices under the influence of external electric field. Electronic polarization occurs at even higher frequencies when an electric field shifts the positively charged nucleus from the negatively charged electron cloud which results in a manifestation of weak local electric field [29]. When considering only the microwave spectrum as the target frequency range, the most prominent mechanism that influences permittivity value is the dipolar polarization.

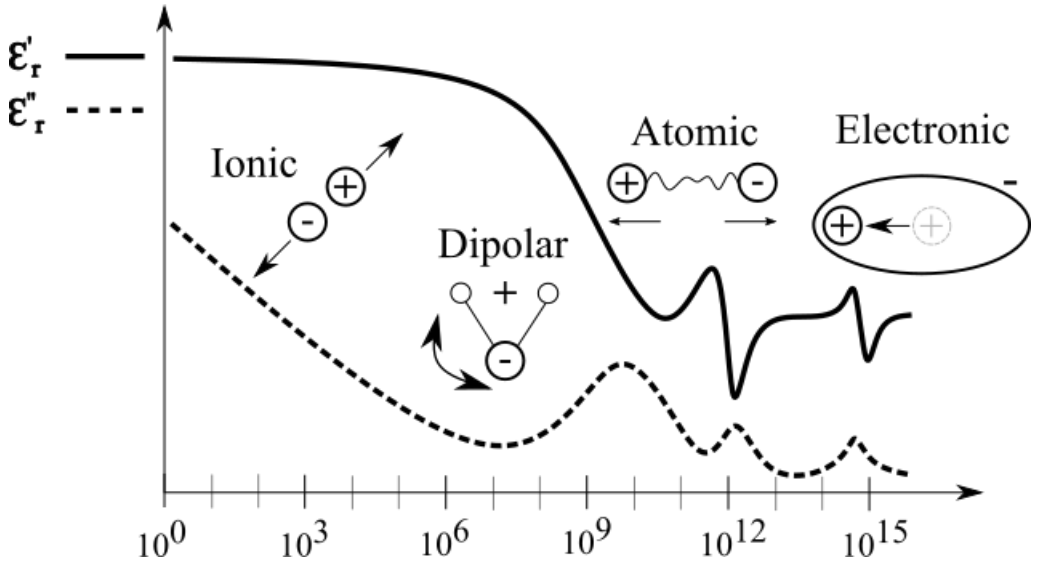

Figure 2.2. Dielectric polarization mechanisms happening under an external electric field of varying frequency. Adapted from [30].

The **dielectric relaxation** is the result of the lag between the movement of dipoles and the change of external electric field. All of the theoretical and empirical models representing the dielectric relaxation phenomena are based on three parameters:

- **static permittivity** ϵ_s is the relative permittivity of a material at sufficiently low frequencies where there is no phase difference between the polarization of dipoles and electric field,
- **infinite permittivity** ϵ_∞ is the relative permittivity at sufficiently high frequencies so that the dipole orientations are not influenced by electric field as its period is negligible compared to the relaxation time of the dipoles,
- **relaxation constant** τ is the time required for a polarized system to return to 1/*e* of its random equilibrium value.

Debye relaxation model defines the dielectric relaxation of an idealized dielectric material to the alternating electric field [31]:

$$\epsilon_r = \epsilon_{r\infty} + \frac{\epsilon_{rs} - \epsilon_{r\infty}}{1 + i\omega\tau} \tag{2.12}$$

where $\omega = 2\pi f$ is the angle frequency in s^{-1}.
Debye relaxation model is based on a single relaxation time and, although showing excellent agreement with the empirical data for the polar liquids, is not adequate for most solid dielectric materials because it is too simplified. **Cole and Cole** [32] have constructed empirical relation based on the dielectric relaxation in polymers which have broader dispersion curves and lower maximum loss:

$$\epsilon_r = \epsilon_{r\infty} + \frac{\epsilon_{rs} - \epsilon_{r\infty}}{1 + (i\omega\tau)^{1-\alpha_{CC}}}\,, \tag{2.13}$$

where α_{CC} is a value between 0 and 1. When α is 0, the Cole-Cole model equals to Debye model. In all other cases, the relaxation expands over a wider frequency range when compared to Debye model. When the broadening of the dispersion curve is asymmetrical, it is more appropriate to use the **Cole-Davidson** relaxation model [33]:

$$\epsilon_r = \epsilon_{r\infty} + \frac{\epsilon_{rs} - \epsilon_{r\infty}}{(1 + i\omega\tau)^{\beta}}\,, \tag{2.14}$$

where β is also in the 0 to 1 range and it reduces to the Debye equation for $\beta = 1$. In other cases, the dispersion curve will become asymmetrical. **Havriliak-Negami** [34] relaxation model adds two exponential parameters to Debye equation which makes it a better fit for most of the experimental results:

$$\epsilon_r = \epsilon_{r\infty} + \frac{\epsilon_{rs} - \epsilon_{r\infty}}{(1 + (i\omega\tau)^{\alpha_{HN}})^{\beta}}. \tag{2.15}$$

Again, α corresponds for the expansion of the relaxation, while β accounts for asymmetry. With β equaling to 1, Havriliak-Negami relaxation model reduces to Cole-Cole model in Eq. 2.13.

Relative dielectric permittivity dependence on temperature stems mostly from the temperature dependent relaxation time τ. As the temperature increases, the relaxation time decreases. Higher temperatures decrease the real part of the dielectric permittivity and decrease and shift the peak of the imaginary part of dielectric permittivity towards higher frequencies [31] as shown in Figure 2.3.

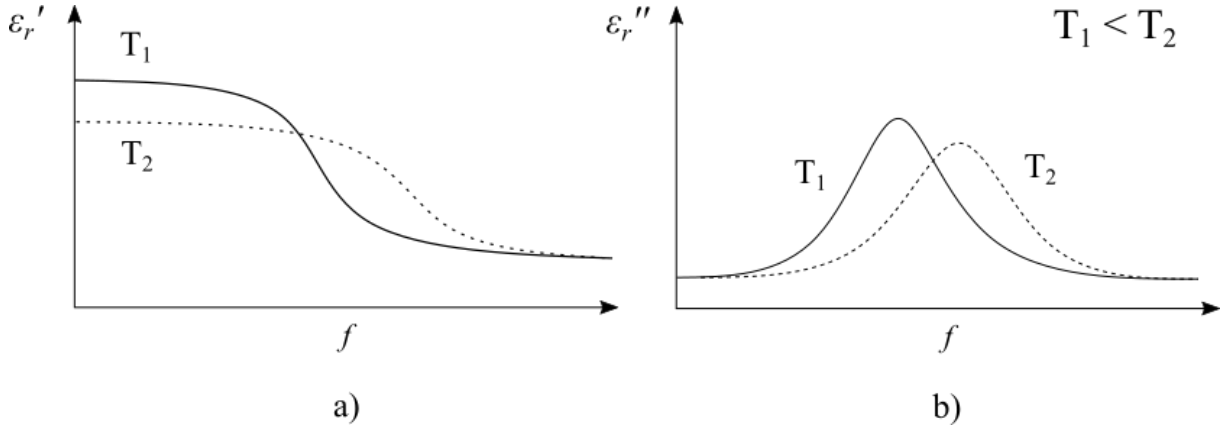

Figure 2.3. Real (a) and imaginary (b) part of complex permittivity plotted as a value of frequency for lower temperature T_1 and higher temperature T_2

Complex permittivity can also be graphed on a **Cole-Cole diagram** [32] which plots the real part of relative permittivity ϵ_r' on the horizontal axis and imaginary part ϵ_r'' on the vertical axis with frequency being the independent parameter. The resulting graph is a curve with the frequency moving counterclockwise on the curve. Example of the Cole-Cole diagram is shown in Figure 2.4 with marked static and infinite permittivity on the beginning and the end of the curve.

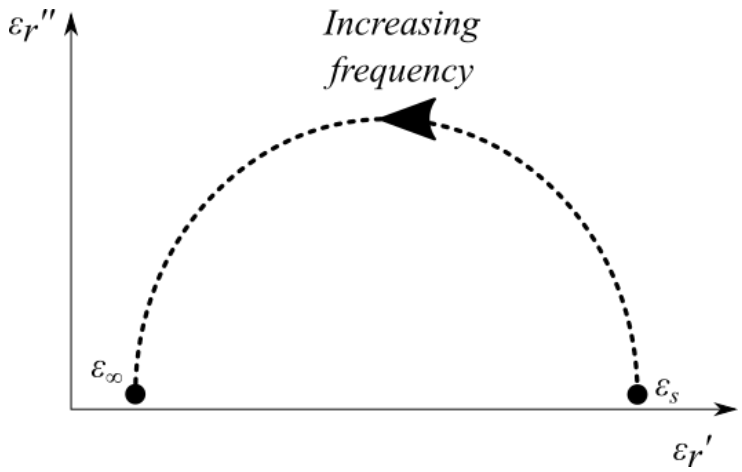

Figure 2.4. Cole-Cole diagram with labeled static and infinite permittivity

3. Overview of dielectric measurement methods

There are a number of different methods for measuring the complex permittivity with each one having its advantages and disadvantages. When performing the measurement, a special attention should be paid to consider the most appropriate method depending on the sample size, material, frequency, etc. In the broadest terms, we can divide the dielectric measurement methods into two categories – resonant and non-resonant methods. Non-resonant methods provide the results in broader frequency range, while resonant methods usually have better accuracy, but are usually limited to narrow spectrum or even a single frequency. High impedance environments are more suited for resonant techniques as opposed to broadband techniques [30]. Non-resonant methods can be further divided by the measured scattering matrix parameter (S parameter) into reflection and transmission/reflection methods. **Scattering parameters** are used to describe the propagation behavior of an N-port linear microwave networks. Example of a two-port network scattering matrix is:

$$\bar{S} = \begin{bmatrix} S_{11} & S_{12} \\ S_{21} & S_{22} \end{bmatrix}. \tag{3.1}$$

Each scattering coefficient represents one possible input/output combination. S_{11} and S_{22} correspond to the input and output reflection coefficient, respectively, while S_{12} and S_{21} represent reverse and forward transmission, respectively. *S*-parameters are usually measured with the vector network analyzer (VNA). Reflection methods measure S_{11} parameter, while transmission/reflection methods also measure S_{22} parameter. This work will give a short overview of each method in the next sections. The methods are arbitrarily organized into three groups: **reflection methods**, **resonant methods**, and **transmission/reflection methods**.

3.1. Reflection methods

Reflection methods include all of the methods where the permittivity is extracted from the reflection due to the impedance mismatch. Impedance mismatch arises from a MUT inserted in the transmission path in a controlled manner. In a reflection method, the measurement fixture is usually carefully designed to have specific desirable characteristics for the intended measurement application.

3.1.1. Open-ended aperture probe

This technique encompasses both coaxial line and open waveguide measurements. Both of these methods are nondestructive and broadband, with open waveguide methods preceding the usage of coaxial lines for measurement. Open-ended aperture probe technique and its solution was first established by Bailey and Swift in 1968 [35] and it included a circular waveguide with an infinite flange radiating into a lossy dielectric backed by a ground plane. As the waveguide presents additional frequency limitations with its cutoff frequency on the lower limit and higher order modes on the upper limit, it was not a perfect choice. Furthermore, waveguides are too large and thus impractical for frequencies lower than a few gigahertz. That is why today the open-ended technique is mostly used with a coaxial probe. The probe is connected with a network analyzer that excites the coaxial line with a TEM wave while the open end of the coaxial cable is in contact with a sample of material under test (MUT), as shown in Figure 3.1. The characteristic impedance of the coaxial line differs from the impedance of the sample which causes the reflection detected by the network analyzer. Dielectric properties are then extracted from the amplitude and the phase of the measured reflection coefficient. Depending on the size

of the probe, the working frequency range can vary from low MHz values to tens of GHz. This technique is suitable for lossy materials, so it is usually used for biological tissue research as tissues have a high percentage of water content which increases their lossiness. Detailed measurement principle of the open-ended coaxial probe will be described in the next chapter.

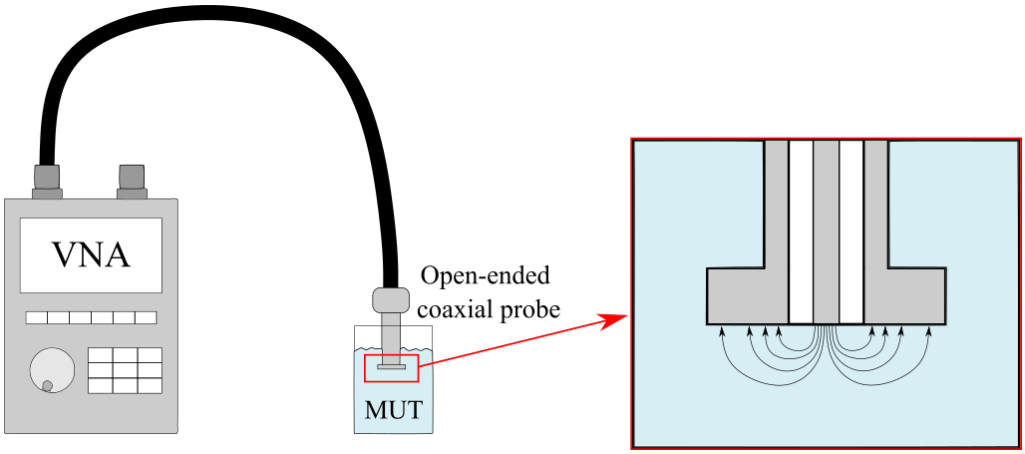

Figure 3.1. Open-ended coaxial probe measurement setup

3.1.2. Monopole antenna probe

This technique utilizes a monopole antenna to transmit electromagnetic waves into a medium of unknown permittivity. This method is best suited for liquid samples as the monopole antenna needs to be immersed. The underlying theory is that the radiation properties of a monopole will change after immersion. The change is observed in the input impedance, particularly reflection coefficient that is easily measurable with the VNA. The expectation is that the MUT around the monopole antenna will contain the antenna's radiation field. This technique was first developed by Smith and Nordgard [36] where the monopole antenna was fed by a coaxial transmission line as shown in Figure 3.2. Examples of de-embedding algorithms which show good experimental results are given by Olson and Iskander [37], Moussa *et al.* [38], He and Shen [39], Hasan and Peterson [40] to name a few.

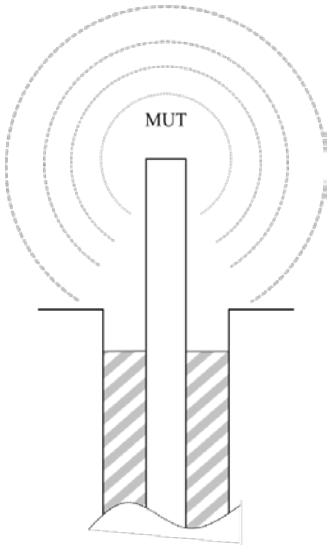

Figure 3.2. Monopole antenna probe

3.1.3. Shorted probe

This category includes coaxial lines and waveguides with the MUT inserted in the end of the line, terminated by a short circuit. This approach was pioneered by Roberts and Von Hippel in 1946 [41]. While the method is simple in practice, its disadvantages comprise the calculations which include solving transcendental equations and additional corrections to acquire accurate results. Additionally, sample thickness influences the results so multiple measurements need to be made to find the optimal sample thickness which was confirmed in 1986 by an uncertainty analysis done by Chao [42]. Variation of this technique was suggested by Saed *et al.* in 1990 [43] which included a cylindrical cavity completely filled with MUT at the end of a coaxial line. Because the cavity is in its non-resonant state, the dielectric properties of the sample are calculated exclusively from the measured reflection coefficient.

3.2. Resonant methods

Resonant methods include many variations of measurement techniques such as **cavity perturbation**, **planar resonator**, **open resonator**, **split cylinder resonator**, etc. They are all based on the measurement of the resonant frequency and the quality factor of the resonator. Because the resonant frequency is easily identifiable from S-parameters as the frequency at which the losses are minimal, the only unknown variable is de-embedding the quality factor *Q* from the measurement results. One of the ways to define **quality factor** is as a ratio of the energy stored to the energy dissipated. In the context of dielectric resonators, quality factor equals to:

$$Q = \frac{\epsilon'_r}{\epsilon''_r} = \frac{1}{\tan(\delta)} \tag{3.2}$$

where the loss tangent *tan*(δ) is already defined in Eq. 2.11. Therefore, loss tangent of the material is calculated from the quality factor, while the dielectric constant of the sample is calculated from the resonant frequency of the resonator.

3.2.1. Resonant cavity perturbation technique

Resonant cavity is a structure that has a large quality factor and resonates at a specific frequency. Permittivity of the sample is calculated from the difference between empty and loaded resonant cavity characteristics, mainly quality factor Q and resonance frequency f_0 [30]. The stronger the electric field in a resonator, the greater is the effect on the resonant frequency. Quality factor can be defined as [44]:

$$Q = 2\pi f \frac{W}{P} \tag{3.3}$$

where:

W is the total stored energy and
P is the power dissipation of the resonator.

Introducing a dielectric sample increases the total stored energy in the resonant cavity, changes the quality factor and shifts the resonant frequency, with the exact values depending on the permittivity of the MUT. The increase in accuracy and sensitivity of this method is obtained by manufacturing the cavity with highly conductive materials which makes the perturbation greater [44].

Cavity perturbation variations include material perturbation [45] depicted in Figure 3.3a, or complete change of the cavity wall with MUT also known as endplate perturbation [46] depicted in Figure 3.3b. Out of those two methods, cavity wall perturbation is mostly used to measure the surface resistance of conductors which leaves the material perturbation as the method of choice for measuring the permittivity of dielectric materials.

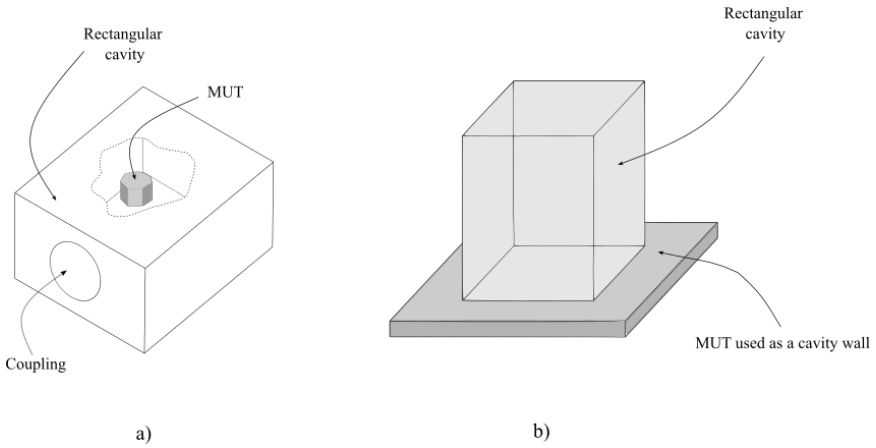

Figure 3.3. a) Cavity perturbation with a small object b) Cavity wall perturbation

3.2.2. Open resonators

The method for the permittivity measurements using an open resonator was first proposed and successfully developed by Culshaw and Anderson in 1962 [47]. This method is best suited for thin, low-loss materials in the millimeter range. A well-known example of the setup is the **Fabry-Perot resonator** which consists of two separate mirrors, one being concave and including a coupling aperture, while the other can be either concave or flat depending on the implementation. Concave mirror(s) help focus the EMFs towards the MUT and therefore reduce the measurement uncertainty [48]. Fabry-Perot resonator setup with one concave and other flat or concave mirror is shown in Figure 3.4. There are two variations of measurements done with

Fabry-Perot open resonator: the frequency variation technique with fixed cavity length and the cavity length variation technique with fixed frequency. This method is generally applied on small samples at high frequencies such as 35 GHz [49], 60 GHz [50], 100 GHz [51], etc.

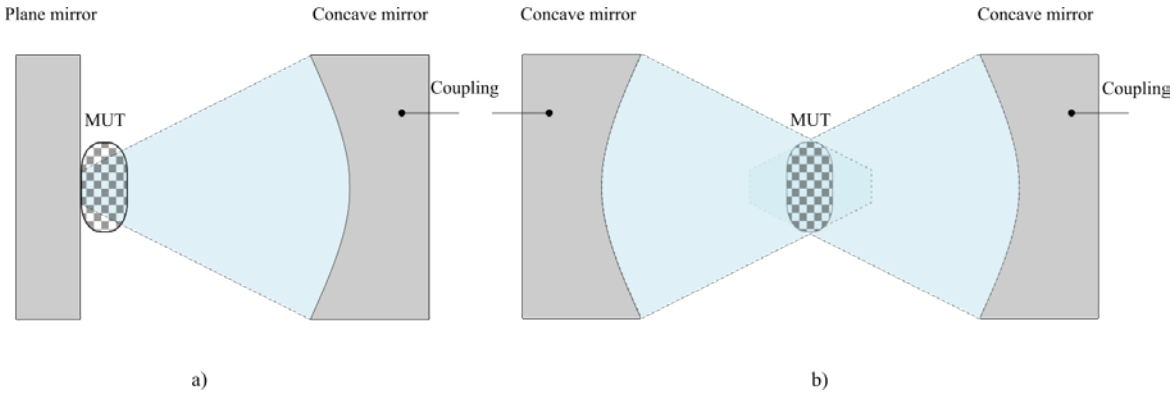

Figure 3.4. Fabry-Perot resonator with a) one flat and one concave mirror b) two concave mirrors

3.2.3. Split Cylinder Resonator

Split cylinder resonator is a cylindrical resonant cavity that is separated into two halves with a gap in between, hence split. One half is fixed, while the other is adjustable and allows for different gap sizes. The gap holds the MUT so, consequently, varying gap size allows for MUTs of different sizes and makes the method suitable for nondestructive measurements. Coupling loops are used in both halves to excite the resonator. Simplification of the setup is depicted in Figure 3.5. Knowing the sample thickness and resonator length while measuring S-parameters allows for a calculation of complex permittivity [30]. This method was first proposed by Kent in 1998 [52] to measure ceramic materials and was valid only for the TE_{011} mode, but is now expanded with other higher-order TE modes [53]–[55].

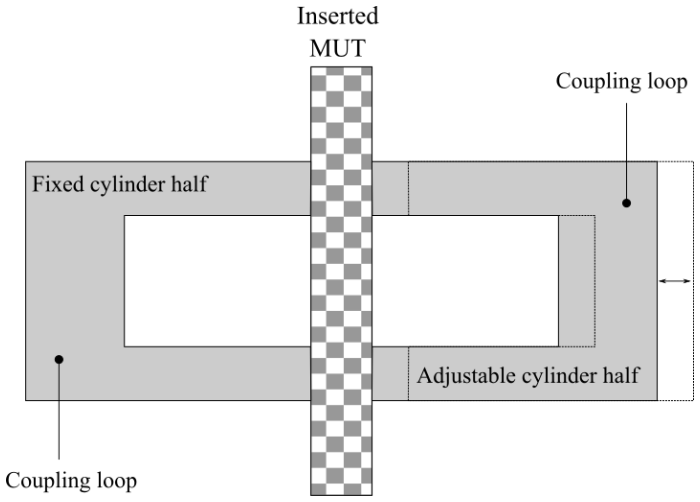

Figure 3.5. Split cylinder resonator with inserted MUT. Adapted from [30].

3.2.4. Split Post Dielectric Resonator

This type of dielectric resonator has a higher quality factor and a better thermal stability than resonant cavity. It is also more appropriate for measuring thin samples with low loss. The geometry of this resonator is shown in Figure 3.6. It operates in the $TE_{01\delta}$ mode which only allows for azimuthal electric field component so that the electric field is continuous on the dielectric interfaces [56]. Typical measurements using this technique were made in the range of 1 to 30 GHz. Over the years, it has been shown that the permittivity measurements made with the split post dielectric resonator provide accurate results with relatively low uncertainty [57]–[59]. In order to increase the sensitivity of measurements even further by reducing the inaccuracy of thin film thickness measurements, stacking of films before measurement is performed. Obtained results show that the dielectric loss tangent can be measured with the resolution of the order of $3x10^{-3}$ [60].

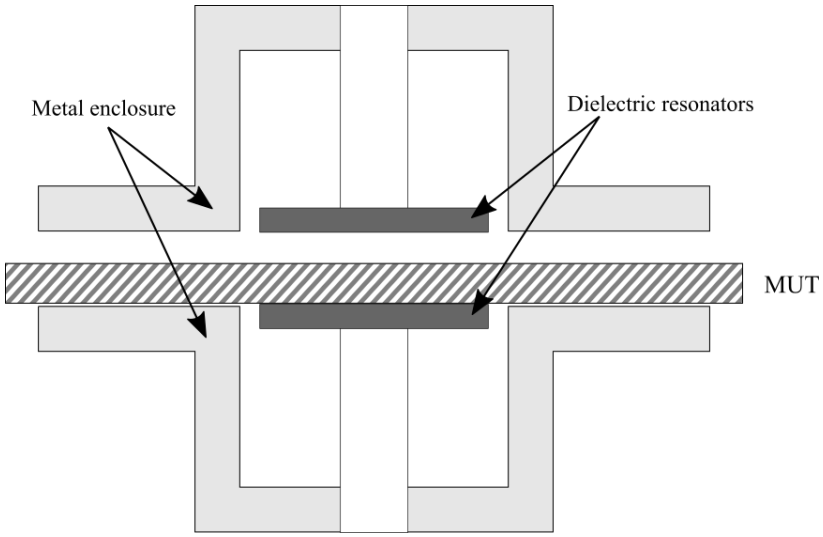

Figure 3.6. Split post dielectric resonator with inserted MUT

3.2.5. Planar resonators

In a planar resonator method, the sample under test is used as a part of the substrate or it completely replaces the substrate. Also, MUT can be used as a superstrate when the manufacturing of the sample does not allow for acceptable substrate geometries. **Stripline resonators** are usually used for measurements of thinner samples because of their higher quality factor, although they cannot accurately measure the imaginary part of complex permittivity ϵ''. The theory behind it was first revealed by Waldron in 1964 [61] and utilized on the rectangular ferrite samples. **Microstrip resonator** methods are analogue to the stripline resonator methods. Microstrip setup includes the ground plane with a dielectric substrate on top of it and a microstrip circuit etched on the conductive layer on top. Air is usually above the circuit so that the effective dielectric constant of the microstrip is related with the amount of the fringing fields in the air and fringing fields in the dielectric substrate as shown in Figure 3.7a. Although most of the electric field is contained in the substrate, there is a weak fringing field above the substrate, nonetheless. If the MUT is put over the microstrip circuit, those fringing fields will penetrate into the MUT. Different configuration and geometries of microstrip resonators are used such as ring resonator [62], rectangular patch resonator [63], resonator with a slotted ground plane [64], open stub resonator [65], etc. Lately, there has been a rise in research and measurements done with split ring resonators (SRR) displayed in Figure

3.7b and its electrical counterpart, the complementary split ring resonators (CSRR) displayed in Figure 3.7c. The SSR exhibits negative effective permeability in the vicinity of resonance, while CSSR exhibits negative effective dielectric permittivity which makes it a good filtering element as it was originally intended to be [66]. Using SSR as a dielectric sensor yields precise results without detailed calculations on small samples that are comparable to the size of the resonator [67]. CSRRs are commonly used for permittivity measurements in microfluidics [68]–[70] as the other permittivity measurement methods are not able to detect and measure such small samples.

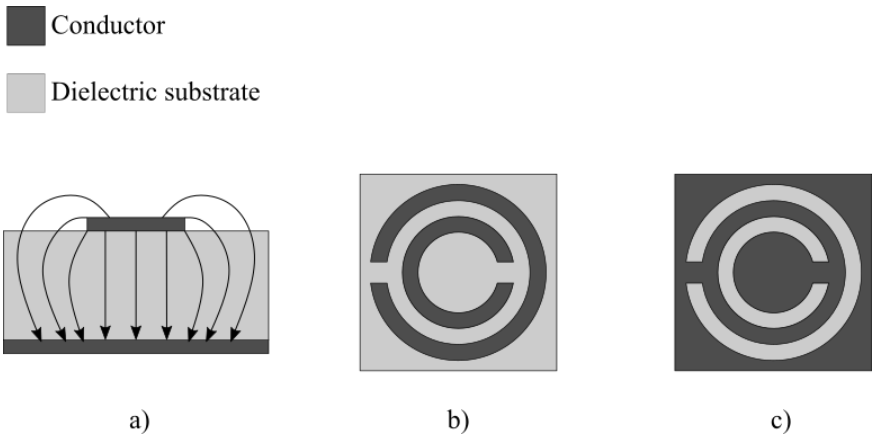

Figure 3.7. a) Fringing fields in a microstrip resonator b) Double split ring resonator c) Complementary double split ring resonator

3.3. Transmission/Reflection methods

Transmission/Reflection methods utilize transmission line concepts, where a piece of dielectric material is inserted at some point along the path of electromagnetic field. This category does not strictly include only the actual transmission lines in the form of a waveguide or a coaxial line, but also air as a transmission medium as realized in the free space method. Network analyzer is used to measure all two-port complex scattering parameters S_{11}, S_{21}, S_{12}, and S_{22}. Some cases require the sample to be cut in a specific way to fully fill the waveguide or a coaxial line which makes selected methods destructive. This set of methods are suitable for materials with medium to high loss.

3.3.1. Coaxial airline

Sample of the material of known thickness is placed into air-filled coaxial line at a known location. Inevitably, impedance mismatch occurs at the interface between the airline and MUT which causes reflections as shown in Figure 3.8. As there are additional reflections, such as those from the connector and airline mismatch, required reflection coefficient from the MUT mismatch plane has to be differentiated in the time domain by gating. Therefore, permittivity results are obtained from the S_{11} parameter which is gated to show only the sample reflection coefficient Γ_{MUT} without possible unwanted reflections from connectors and adapters. As time-domain measurement procedure for transmission/reflection measurements was first described in detail by Nicolson and Ross [71] and Weir [72], it is also known as NRW (Nicolson-Ross-Weir) algorithm. Their algorithm required the transformation of S-parameter plane to the interface with the MUT which added additional uncertainties. The method is best suited for materials with low conductivity to ensure successful transmission. The thickness of the MUT

must be sufficient to have correct results, but multiples of half of the wavelength should be avoided as they cause unwanted resonances. Valuable alternative algorithm was proposed by Baker-Jarvis *et al.* [73] which eliminates the problem of a reference plane position and sample length limitations as the equations are independent of both. Theoretically, the measurements can be made down to 0 Hz. It is crucial that the only mode propagating along the coaxial cable section with the inserted MUT is the transverse electromagnetic (TEM) mode. Therefore, the upper working frequency range is defined by the coaxial line dimensions, with smaller coaxial lines having higher upper frequency limit above which the higher modes begin to evolve. Downside of this method is that the sample must be fabricated in a toroid shape which is not always feasible. Additional measurement uncertainties stem from the potential air gaps between the MUT and the walls of the inner and outer conductor, line losses and coupling to higher order modes.

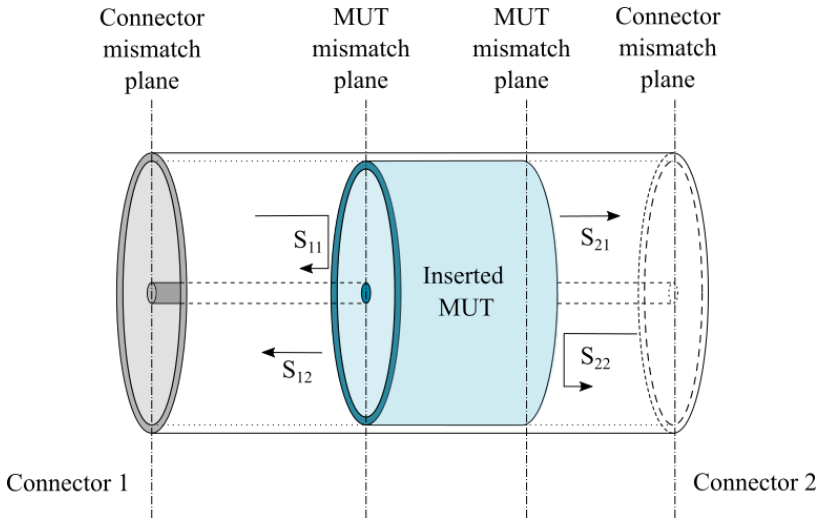

Figure 3.8. MUT placed into coaxial airline with indicated scattering parameters at MUT interfaces.

3.3.2. Hollow waveguide

Similar to the previous technique, the MUT is inserted in a section of waveguide which serves as a transmission line. The complex scattering parameters are measured while using the same data processing algorithms for permittivity extraction as described in the previous subchapter. Simplified graphic of this method is visible on the Figure 3.9. Rectangular waveguides are more common than circular due to the ease of fabrication of a rectangular sample versus a cylindrical one which is also one of its main benefits over a coaxial airline method. Important difference of the hollow waveguide setup is the existence of the cutoff frequency. The cutoff frequency should be known precisely as it is included in the analytic model. Small imperfections in the manufacturing of the waveguide, e.g., distorted corners, lead to the shift in the expected cutoff frequency for the geometry. A solution was proposed by the introduction of the effective waveguide width by Anis *et al.* [74] which aims to correct the accuracy of the setup. The method showed good agreement when measuring low loss materials even for thin samples [75], [76].

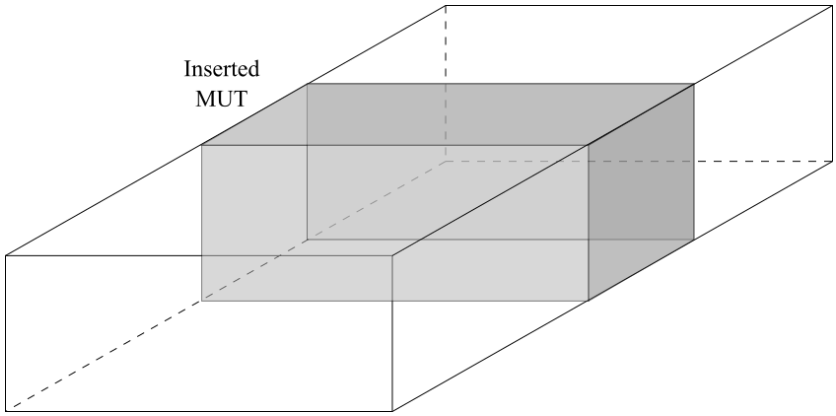

Figure 3.9. MUT placed into hollow rectangular waveguide

3.3.3. Planar Transmission Line

Planar transmission line measurement methods generally utilize test sample as a substrate or superstrate. As a substrate, its effect on the transmission line is obvious, but when used as a superstrate and placed over the transmission line, the sample changes the effective permittivity of a planar transmission line. Permittivity of the measured sample is determined from the difference between unloaded and loaded line. The three typical types of planar transmission lines are microstrip, stripline, and coplanar line as shown in Figure 3.10. **Microstrip line** is the simplest and most prevailing method from this group. MUT is usually used as a substrate because the electromagnetic properties of the substrate are easily obtained from the measured transmission and reflection coefficient of the line. The math behind the extraction of electromagnetic properties was detailed in [77]. As mentioned, MUT can also be used as a superstrate and loaded onto microstrip line as shown by Queffelec *et al.* in 1994 [78] and 1998 [79]. Advantage of this method is that virtually no sample preparation is required. In the **stripline structure**, the MUT can be inserted above or below the center strip. Benefit of the stripline structure is the possibility of broadband measurements because of the higher cutoff frequency [44]. In 1986 Barry [80] introduced a broadband permittivity and permeability measurement technique that involves symmetrical strip transmission-line fixture loaded with the MUT from both sides. Achieved accuracy was within the 5% range. Increased sensitivity is achieved by using asymmetrical stripline method [81], [82] which eliminates the upper ground plane and the need to surround the stripline with MUT from both sides. Lastly, **coplanar line** is also used as a measurement fixture in the similar way. MUT can be used as a substrate with the included inconvenience of sample preparation, but is more feasible when used as a superstrate as described in [83].

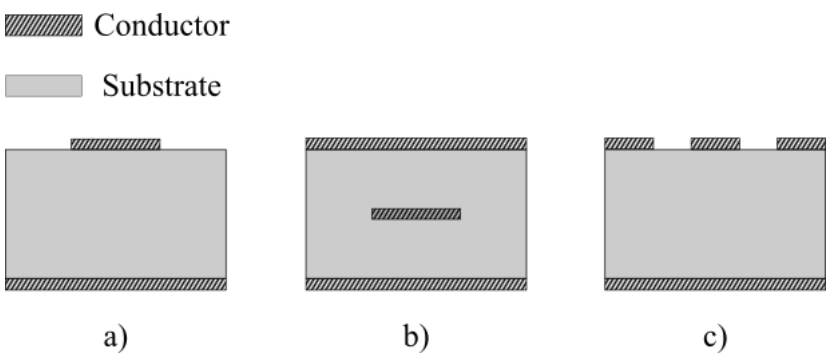

Figure 3.10. Examples of planar transmission lines a) microstrip b) stripline c) coplanar line

3.3.4. Free-space technique

The MUT is placed between the two antennas for a non-contact measurements under free-space conditions. There are two variations of this technique as shown in Figure 3.11: **transmission** and **reflection configuration**. Both configurations are suitable for the measurements made on high-temperature or corrosive samples because the sample is isolated from the rest of the setup. To obtain accurate complex permittivity results, sample must be kept at a sufficiently large distance from both antennas to ensure that it is situated in antennas' far fields. This method works best with low loss materials, while lossy MUTs should be kept thin to allow for transmission to take place. Nevertheless, the samples should not be significantly smaller than the wavelength at the operating frequency of the antennas as that can also distort the results. Naturally, the measurement environment should be kept noise-free, preferably done in an anechoic chamber. With the use of time gating, errors of unwanted reflections can be eliminated [84]. Before starting the measurement, a calibration must be performed on the vector network analyzer (VNA). Calibration should also be refreshed for every change in the measurement setup e.g., change in separation distance, antenna height, etc. Some calibration combinations are through-reflect-line (TRL), through-reflect-match (TRM), line-reflect-line (LRL), etc. **Through** standard is achieved by direct transmission between antennas, without MUT between them. **Match** is achieved by placing RF absorber foam of the same size as MUT which, in turn, absorbs all transmitted power, just like a matching load in a transmission line. The **line** calibration standard is obtained by separating the two antennas by a quarter of wavelength of center frequency, while the **reflect** standard is measured with a metal plate between the antennas which is the same size and placement as the MUT will be in the measurements [85].

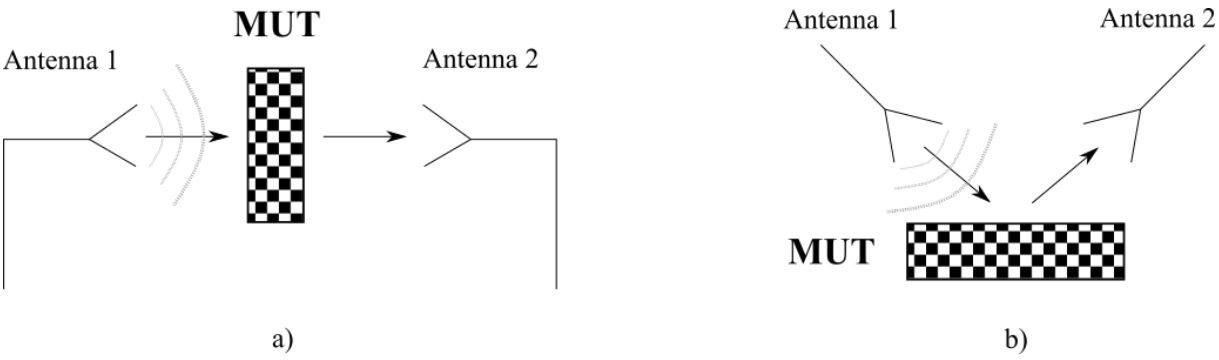

Figure 3.11. Free space measurement technique a) transmission configuration b) reflection configuration

4. Overview of open-ended coaxial probe method

4.1. Introduction

As the need for nondestructive measurements arose, especially in biomedical microwave diagnostics, so did the popularity of the open-ended coaxial probe method. Coaxial probes have already been commercialized and some of the most recognizable manufacturer names are Keysight [86] (formerly the brand names were Hewlett-Packard and Agilent), SPEAG [87], APREL [88], and KEYCOM [89]. Depending on the dielectric kit used, different probes may be used for different types of MUTs, setups and frequency ranges. For example, some measurements benefit from probes that can withstand a wide range of temperatures which makes them suitable for autoclaving or measurements of a very hot or cold materials. Probe size can also be a crucial deciding factor when performing measurements in narrow aperture containers or on small samples. Some probe designs and materials make them resistant to corrosive or abrasive samples. Finally, the probe dimensions are correlated with the operating frequency range, restricting the probe selection within the frequency range of interest.

Figure 4.1. Examples of different open-ended coaxial probes. Probes manufactured by Keysight are displayed in the top row [30]*, while the ones manufactured by SPEAG are shown in the bottom row* [87].

The method is based on the study of the fringing electric field at the open end of the coaxial line and its transformation caused by the lossy dielectric in the contact with the open end. The measured sample is acting as a load to an open end of the coaxial line. To successfully utilize this concept, a full analysis of the admittance at the end of the line must be made. Simplified models neglect the possibility of the probe radiation into the sample and thus do not result in accurate permittivity values for high frequencies or lossy materials [90]. Overview of the de-embedding methods will be given later in Chapter 4.2.

In a coaxial probe at sufficiently high frequencies, both the voltage wave and the current wave have two components propagating towards the load and towards the generator. These two components are usually called incident wave and reflected wave. The reflected wave arises when the incident wave is reflected back from the open end of the coaxial probe. The **voltage**

reflection coefficient at the input of the line of length *z* represents the ratio between the reflected voltage **phasor** V_- and the incident voltage **phasor** V_+ [44]:

$$\Gamma_i = \frac{V_-(z)}{V_+(z)} = \frac{V_{0-}\, e^{-j\beta z}}{V_{0+}\, e^{+j\beta z}}\,, \tag{4.1}$$

where V_{0-} and V_{0+} are the reflected and incident voltage phasors at the load interface and $\beta = 2\pi/\lambda$. The magnitude of the reflection coefficient varies from 0 to 1 depending on the lossiness of the material, while the phase of the reflection coefficient depends mostly on the real part of the relative permittivity. The relationship between the **impedance** and reflection coefficient, both at the input of the line of length *z*, is:

$$Z_i = Z_0 \frac{1+\Gamma_i}{1-\Gamma_i} \text{ or } \Gamma_i = \frac{Z_i - Z_0}{Z_i + Z_0}. \tag{4.2}$$

Input admittance and reflection coefficient at the same point on the transmission line are connected as follows:

$$Y_i = Y_0 \frac{1-\Gamma_i}{1+\Gamma_i} \text{ or } \Gamma_i = \frac{Y_0 - Y_i}{Y_0 + Y_i}. \tag{4.3}$$

Z_0 and Y_0 represent the characteristic impedance and admittance, respectively. Combining the previous equations with the de-embedding equivalent circuit models which will be covered later, one can simply deduce the complex permittivity from the measured reflection coefficient.

4.1.1. Calibration

As the measurements with a coaxial probe are done in a microwave frequency range, the coaxial line cannot be considered an ideal transmission line as there are additional unaccounted reflections and losses. The solution is to consider the coaxial probe as a general two-port network as shown in Figure 4.2. N-port networks are unambiguously defined by their scattering parameters. In case of a two-port network, the scattering parameters are S_{11}, S_{12}, S_{21}, and S_{22}. They link the incident (a_1 and a_2) and reflected (b_1 and b_2) signals from port 1 and port 2 [91]:

$$b_1 = S_{11}a_1 + S_{12}a_2\,, \tag{4.4}$$

$$b_1 = S_{11}a_1 + S_{12}a_2\,, \tag{4.5}$$

or, shown in a scattering matrix:

$$\begin{bmatrix} b_1 \\ b_2 \end{bmatrix} = \begin{bmatrix} S_{11} & S_{12} \\ S_{21} & S_{22} \end{bmatrix} \begin{bmatrix} a_1 \\ a_2 \end{bmatrix}, \tag{4.6}$$

where:

a_1 and a_2 are incident signal waves,
b_1 and b_2 are reflected signal waves,
$S_{11} = b_1/a_1$ with $a_2 = 0$; input reflection coefficient with a matched output,
$S_{22} = b_2/a_2$ with $a_1 = 0$; output reflection coefficient with matched input,
$S_{21} = b_2/a_1$ with $a_2 = 0$; forward transmission coefficient with matched output,

$S_{12} = b_1/a_2$ with $a_1 = 0$; backward transmission coefficient with matched input.

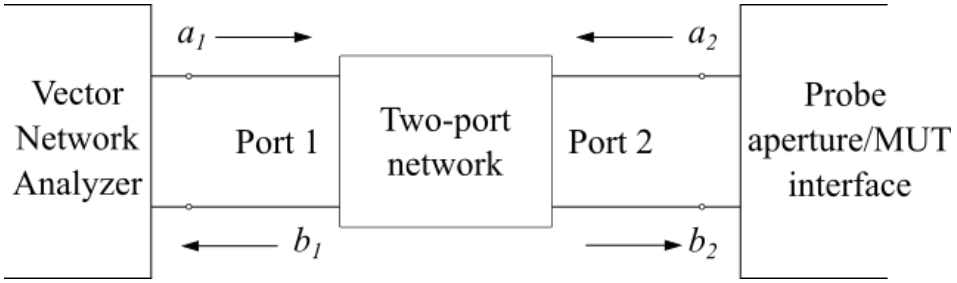

Figure 4.2. OECP treated as a general two-port network with incident (a_1 and a_2) and reflected (b_1 and b_2) signals (adapted from [91]).

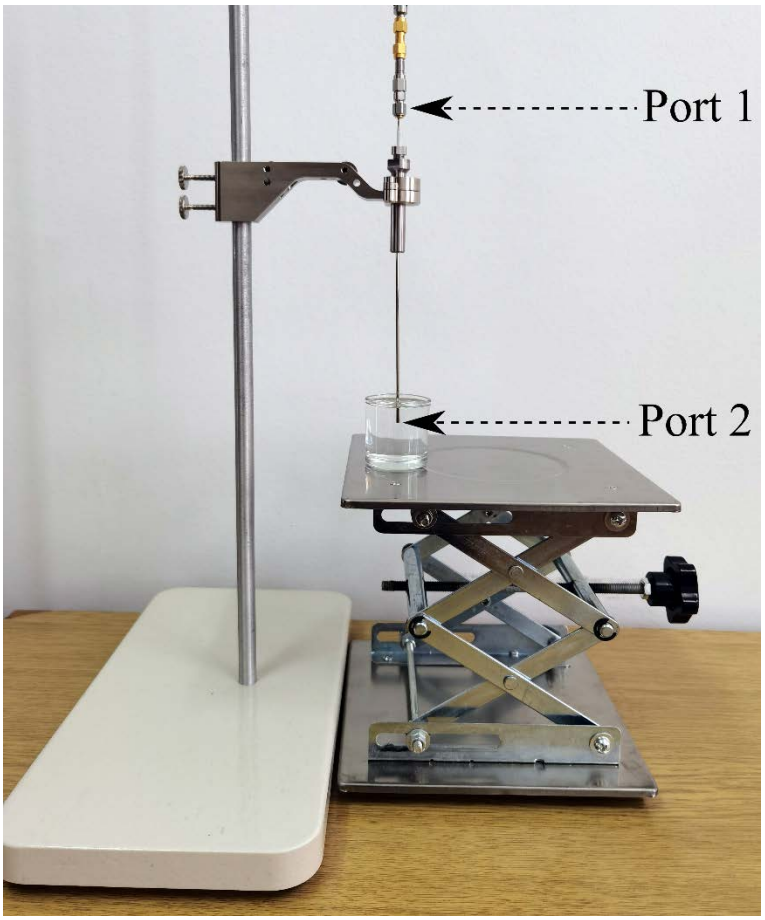

Figure 4.3. OECP measurement setup with Port 1 and Port 2 noted on the image

When measuring the reflection coefficient with a vector network analyzer, the resulting measurements are obtained at the probe coaxial connector (Port 1 noted in Figure 4.2. and Figure 4.3.). For most of the de-embedding model calculations, the reflection coefficient needed in the equations is the one at the plane of the probe aperture/MUT interface (Port 2 noted on the Figure 4.2. and Figure 4.3). When following the previous notation from the matrix Equation 4.6, needed reflection coefficient is $\Gamma_{MUT} = a_2/b_2$, and the one obtained on the VNA is $\Gamma_m = b_1/a_1$. Γ_{MUT} can be calculated from the Γ_m and the previously measured scattering parameters of the two-port network for several known MUTs [91]:

$$\Gamma_{MUT} = \frac{\Gamma_m - S_{11}}{S_{22}\Gamma_m + S_{12}S_{21} - S_{11}S_{22}}\,. \tag{4.7}$$

The number of unknown variables defines the required number of equations which, in turn, defines the needed number of MUTs. For each well-defined MUT (n = 1,2, 3, …, N) it is possible to calculate the exact Γ_{MUTn} using Equation 4.2 or 4.3 and measure the $\Gamma_{mn}\rho_i$ at Port 1. In the case of Equation 4.7, there are three unknown variables that need to be independently determined: S_{11}, S_{22}, and the product $S_{12}S_{21}$. Scattering parameters are then defined as [91]:

$$S_{11} = \frac{\Gamma_{m3}\Gamma_{MUT1}\Gamma_{MUT2}(\Gamma_{m1} - \Gamma_{m2}) + \Gamma_{m2}\Gamma_{MUT3}\Gamma_{MUT1}(\Gamma_{m3} - \Gamma_{m1}) + \Gamma_{m1}\Gamma_{MUT2}\Gamma_{MUT3}(\Gamma_{m2} - \Gamma_{m3})}{\Gamma_{MUT1}\Gamma_{MUT2}(\Gamma_{m1} - \Gamma_{m2}) + \Gamma_{MUT3}\Gamma_{MUT1}(\Gamma_{m3} - \Gamma_{m1}) + \Gamma_{MUT2}\Gamma_{MUT3}(\Gamma_{m2} - \Gamma_{m3})}, \tag{4.8}$$

$$S_{22} = \frac{\Gamma_{MUT1}(\Gamma_{m2} - S_{11}) + \Gamma_{MUT2}(S_{11} - \Gamma_{m1})}{\Gamma_{MUT1}\Gamma_{MUT2}(\Gamma_{m2} - \Gamma_{m1})}, \tag{4.9}$$

$$S_{12}S_{21} = \frac{(\Gamma_{m1} - S_{11})(1 - S_{22}\Gamma_{MUT1})}{\Gamma_{MUT1}}. \tag{4.10}$$

Accordingly, calibration is performed by measuring the response of known independent standards, usually open, short, and a well-defined load. Calibration helps to virtually shift the measurement reference plane from the probe coaxial connector to the probe aperture/MUT interface, correcting for systematic errors at each frequency of interest. Systematic errors are caused by imperfections in the measuring instrument and the test setup. Three types of systematic errors that calibration aims to account for are: directivity, frequency response, and source match errors. **Directivity errors** are caused by the portion of the incident wave arriving back to the VNA without reflecting from the sample. **Frequency response errors** occur when there is path loss and time delay between the incident wave detector and reflected wave detector. **Source match errors** appear as the wave initially reflected from the MUT recombines with the incident wave after additional unwanted reflection from the unmatched signal source [92].

To eliminate the influence of transmission-line discontinuities caused by the setup drift due to the change of the temperature, cable movement and other unwanted instabilities that occur after the initial calibration, calibration should be refreshed with any one of the calibration standards regularly. **Refreshing the calibration** provides a first order correction to the initial estimates of the systematic errors to account for possible perturbation. Three of the most common calibration standards are open, short, and deionized water as they provide a wide range of permittivity values [93]. The *open* model has a very good agreement with the open calibration standard unless the probe surface has been damaged. Deionized water is a standard calibration liquid, thoroughly measured and well defined previously. It is, however, important to use pure deionized water without any contaminants that could influence the results, to ensure accurate calibration. The downside of using water as a calibration liquid is its low boiling point which hinders measurements in high-temperature environments. When performing calibration in high-temperature setups, a better choice is a standard ceramic material with well-defined permittivity [94]. Lastly, the *short* standard is more variable as its repeatability is dependent on the proper contact of the shorting material with the probe aperture [95]. Some of the other standard reference liquids used instead of water are isopropyl alcohol, methanol, ethanol, etc. Generally, the calibration standards should be chosen so that two of them have reflection coefficients on the opposite side of spectrum and the third one is midway between the first two [96]. That is why Fornes-Leal *et al.* [97] have tested their enhanced calibration model with one of the

following polar liquids instead of water: methanol, ethanol, and 2-propanol. They hoped to better characterize the intermediate permittivity region with a polar liquid of lower permittivity. Uncertainty analysis in the 0.5 to 8.5 GHz frequency band showed a lower uncertainty is accomplished when the added calibration liquid has similar properties to the measured material. That is why adding methanol as a calibration liquid was beneficial for the measurements of high water content materials, while addition of ethanol improved accuracy of measurements of low water content materials.

Wagner *et al.* [98] suggested that, to improve the accuracy of the OECP technique, one should combine open-water-short calibration at lower frequencies with open-water-standardized liquid at higher frequencies. The boundary being around 500 MHz due to the inaccuracy of the implementation of the short standard. Aminzadeh *et al.* [99] experiments showed how important it is to keep the probe aperture below the calibration liquid surface. They tested surface calibration and dip calibration with immersion of around 1 cm on deionized water as their calibration liquid of choice. Results showed that surface calibration does not give accurate enough results and affects the measurement results differently depending on the permittivity of the MUT. Otto and Chew [100] proposed an improved calibration procedure that utilizes *short*, *open* and a short-cavity termination. That way, they hope to avoid the calibration dependency on a known dielectric sample as its actual permittivity is variable with the temperature, purity, and many other factors. The caveat is that the size of the cavity must be chosen to ensure that its reflection coefficient will be different from other two calibration standards. Resulting calibration should then only rely on the geometry of the probe.

4.1.2. Effects of flange

Generally, probes are manufactured either with or without (Figure 4.4a) a flange. In most of the idealized flanged OECP models, ground flange extends to infinity (Figure 4.4c) and has infinite conductance which ensures that the transverse electric field is forced to be zero at the flange boundaries. It is obvious that the real-life probe models have their limitations, especially when considering practical probe designs and flange sizes. Zheng and Smith [101] first reported improvements in permittivity measurements when using a finite conductor flange (Figure 4.4b). Flange had a diameter that was ten times larger than the external diameter of the outer conductor. Measured results in the 0.5 – 5 GHz frequency spectrum showed that the flanged probe provided more accurate results because the flange enforced field boundary conditions inside the MUT. Additionally, the usage of a flanged probe yielded better results for simplified two-term admittance equation compared to the three-term equation which simplifies the postprocessing step. Their results were later confirmed in De Langhe *et al.* [102].

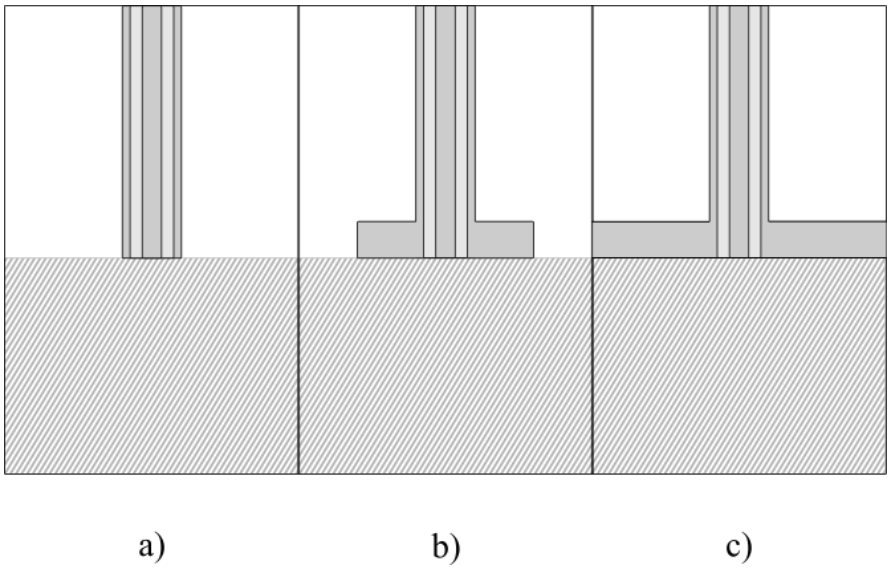

Figure 4.4. a) Flangeless OECP b) OECP with finite flange c) OECP with infinite flange

Okoniewski *et al.* [103] have investigated the effects of a finite flange on a computational model of a coaxial probe having a 3.6 mm outer diameter. Probe was modeled using Method of Moments (MoM) and Finite Difference Time Domain (FDTD) technique. Simulations were performed at three discrete frequency points: 2.117, 5.098 and 10.07 GHz. The difference between external radius of flange and external radius of outer conductor varied from 1.8 mm to 8.8 mm. As expected, values for the finite flange model converged to infinite flange asymptote for each frequency tested as the flange radius extended. For flange diameters larger than $\lambda/2$, measured reflection coefficient differed by less than 0.25% from the infinite flange. They have also tested the difference in measurements for three flange thicknesses: 0.25 mm, 0.5 mm, and 1 mm. The results showed that the flange thickness did not have a noticeable influence on measurement results beyond the shift of the location of a scattering point distant from the aperture.

Fallahi *et al.* [104] have additionally quantified the effects of flange truncation compared to the infinite flange model. When the samples are lossy and the radius of the flange is adequate, the effect on the measurement results is insignificant as the fields get sufficiently attenuated from the probe open aperture to the flange boundaries. On the other hand, when measuring lossless samples, the effect of a smaller flange is more visible. In their work, they have demonstrated the effects of flange resonance with FDTD simulations that happen when an unattenuated field in an almost lossless sample reflects from the flange boundaries which leads to oscillations in measurement results. When observing the graphs at Figure 4.5., the reflections are clearly visible in both the real and imaginary parts of the reflection coefficient at the probe aperture. To solve this issue, they proposed a setup with a lossy platform below the sample which aims to prevent the propagation of the fields thus removing the visible flange resonances. Naturally, further analysis should include the multilayer model as the lossy platform should be accounted for in the results.

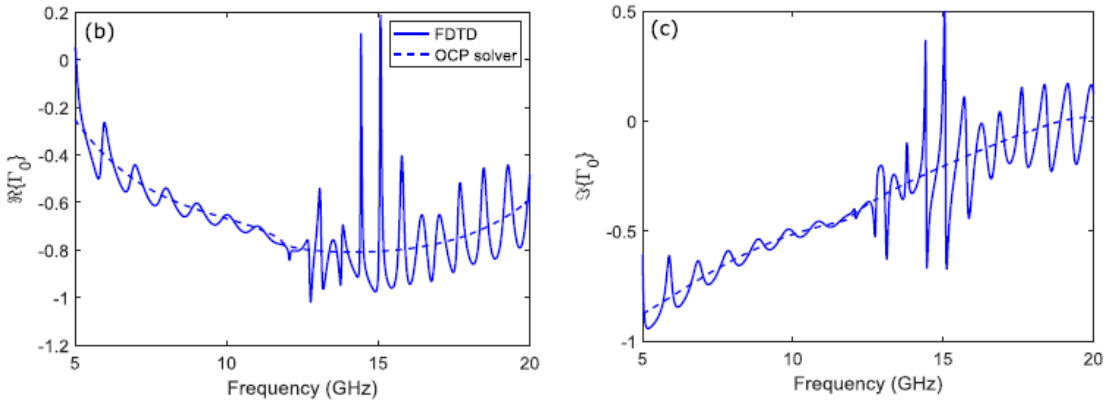

Figure 4.5. a) Real and b) Imaginary part of reflection coefficient with visible flange resonances taken from [104]

4.2. De-embedding methods and models

When using VNA to characterize the admittance of OECP, it is expected that the measured frequency dependent admittance under steady state conditions will be indistinguishable from the one of a linear network such as a parallel or series combination of resistors, inductors, and capacitors. General equivalent circuit for the open-ended coaxial probe method is shown in Figure 4.6a. The impedance $Z(\epsilon_r)$ or the admittance $Y(\epsilon_r)$ of the coaxial aperture are a function of the relative permittivity of the sample under test. Because the load is connected in parallel with the rest of the circuit, it is more manageable to handle the de-embedding using only admittance of the equivalent circuit. In the past years, many variations of equivalent models of the probe aperture admittance have been created. This work will describe the four most common ones in the next sections. They are capacitive model (Figure 4.6b), antenna (radiation) model (Figure 4.6c), rational function model and virtual transmission line model (Figure 4.6d).

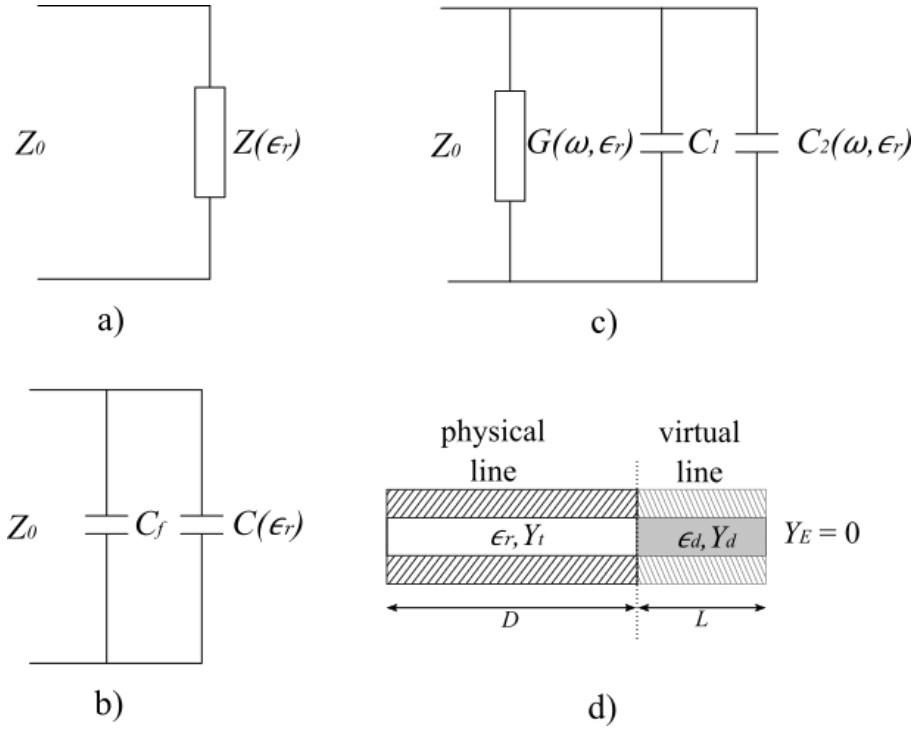

Figure 4.6 a) General equivalent circuit for the open-ended coaxial probe b) Capacitive model c) Antenna (radiation) model d) Virtual transmission line model

4.2.1. Capacitive model

In the capacitive model, the aperture impedance is substituted with two capacitive elements $C(\epsilon_r)$ and C_f. C_f represents the capacitance arising from the fringing fields that partly propagate in the dielectric of the coaxial line and is not depended on the MUT's permittivity, while $C(\epsilon_r)$ is linked to the MUT's permittivity and the capacitance measured when the probe is terminated with air C_0:

$$C(\epsilon_r) = \epsilon_r C_0 \,. \tag{4.11}$$

With the complex impedance specified, the reflection coefficient at the probe aperture/MUT interface is easily obtained using the equation:

$$\Gamma_{MUT} = |\Gamma|^{j\Phi} = \frac{1 - j\omega Z_0 (C(\epsilon_r) + C_f)}{1 + j\omega Z_0 (C(\epsilon_r) + C_f)} \,. \tag{4.12}$$

After substituting the value for $C(\epsilon_r)$ from Eq. 4.11. into Eq. 4.12., ϵ_r is extracted from:

$$\epsilon_r = \frac{1 - \Gamma_{MUT}}{j\omega Z_0 C_o (1 + \Gamma_{MUT})} - \frac{C_f}{C_0} \,. \tag{4.13}$$

Because there are two unknown variables, C_f and C_0, one needs two equations to solve them. In other words, two calibration mediums with well-known dielectric properties are needed to properly perform the calibration procedure and extract the values of C_f and C_0. Additionally, since this model requires the reflection coefficient to be determined at the aperture plane from the measured reflection coefficient at the probe connector plane, further calculation must be

performed to shift the phase of the reflection coefficient accordingly [105]. While the total capacitance of the aperture in the air (C_f + C_0) can be both calculated analytically and determined experimentally, the differentiation of the two capacitances can be only determined experimentally. The upper frequency limit of this model is constrained by the unwanted radiation effect that occurs when the dimensions of the open end of the probe are comparable to the operating wavelength. Because the radiation effects are not accounted for in this model's equivalent circuit, the errors in the results are inevitable [106]. Detailed visualization of the frequency limitations of this model was given by Ellison and Moreau in 2008 [107]. Although also applicable on other empirical models, the focus was specifically on the capacitive model or, as they refer to it, lumped capacitor model. The result was a method that helps determine whether the frequency range and permittivity interval for a chosen model gives the results within specified acceptable deviation from theoretical values. The analytic expressions and the mathematical solutions of their model include extended transformations of integrals that are too extensive to list here.

4.2.2. Antenna (radiation) model

An open-ended coaxial probe can be considered as a functional antenna radiating in the lossy medium, therefore this model is called antenna or radiation model. It substitutes the admittance of the probe aperture with the capacitance C_1, C_2, and conductance G connected in parallel. Equivalent circuit from Figure 4.6c yields the following formula for a normalized admittance at the probe aperture plane:

$$\frac{Y}{Y_0} = j\omega C_1 Z_0 + j\omega Z_0 C_2(\omega, \epsilon_r) + Z_0 G(\omega, \epsilon_r). \tag{4.14}$$

C_1 arises from the fringing fields inside of the probe and corresponds to the C_f from the previous capacitive model. For lower frequencies that result in large wavelengths when comparing to the probe dimensions, we can consider C_2 as frequency independent and simplify it to $C_2(\omega, \epsilon_r) = \epsilon_r C_0$. $G(\omega, \epsilon_r)$ includes the effects of radiation conductance and equals to $G_0 \epsilon_r^{5/2}$ where G_0 is the free-space radiation conductance [111]. That allows for rewriting Eq.4.14 as:

$$\frac{Y}{Y_0} = j\omega C_1 Z_0 + j\omega Z_0 C_0 \epsilon_r + Z_0 G_0 \epsilon_r^{\frac{5}{2}}. \tag{4.15}$$

Because there are three unknown variables: C_1, C_2 and G_0, calibration must be performed with three well-defined materials before performing the measurement on the unknown MUT. Because of the fifth order, there are five possible solutions, but only one of them should have a physical significance (e.g., $\epsilon_r' > 1$). Just like with the previous model, this model also requires the reflection coefficient to be determined at the aperture plane by measurement. [105].

4.2.3. Rational function model

The model is based on a rational function of a full-wave method of moments (MoM). The model includes radiation effects, energy storage in near field region and the evanescent mode effects. The admittance of the aperture model as a function of the complex permittivity of the MUT is given by [112]:

$$\frac{Y}{Y_0} = \frac{\sum_{n=1}^{N}\sum_{p=1}^{P}\alpha_{np}(\sqrt{\epsilon_r})^p s^n}{1 + \sum_{m=1}^{M}\sum_{q=1}^{Q}\beta_{mq}(\sqrt{\epsilon_r})^q s^m}\ , \tag{4.6}$$

where:

α_{np} and β_{mq} are the coefficients of the model which depend upon the geometry of the line,
s is the Laplacian variable $s = \sigma + j\omega$,
Y_0 is the characteristic admittance of the coaxial probe.

The complex permittivity of the MUT is obtained by inverting Eq. 4.6 and choosing the appropriate solution from the higher order complex equation. The advantage of this model is that there is no need for calibration with known loads as the parameters α_{np} and β_{mq} are defined by the least squares fit to the computed MoM data. They are tested and valid for the measurements made in the 1 - 20 GHz frequency range and for MUT permittivity ranging from 1 to 80 for ϵ' and 0 to 80 for ϵ''. The model has been validated experimentally by Anderson *et al.* using water as a MUT and measuring up to 18 GHz one year after the model's introduction [113] and later by additionally measuring and confirming with methanol [114].

4.2.4. Virtual transmission line model

This model consists of a virtual transmission line (TL) terminated with an open end that models the MUT. The complex permittivity is calculated from the effective transmission line which models the fringing electric field. Complex admittance at the probe aperture is given by [105]:

$$Y_L = Y_d \frac{Y_E + jY_d \tan(\beta_d L)}{Y_d + jY_E \tan(\beta_d L)}\ , \tag{4.7}$$

where:

Y_L is the admittance at the input of virtual TL,
Y_d is the characteristic admittance of the virtual TL,
Y_E is the admittance at the output of the virtual TL,
β_d is the phase constant in the MUT,
L is the length of the virtual TL.

Because this model assumes an open termination of the virtual TL, Y_E is zero and the input admittance reduces to:

$$Y_L = jY_d \tan(\beta_d L). \tag{4.8}$$

Y_d can be expressed as a function of inner (a) and outer (b) diameter of the coaxial probe and the complex permittivity of the MUT (ϵ_r):

$$Y_d = \frac{\sqrt{\epsilon_r}}{60 \ln\left(\frac{b}{a}\right)}\ . \tag{4.9}$$

Finally, the input admittance from the virtual line can be expressed using admittance Y_t at the interface between the virtual and real TL:

$$Y_L = Y_t \frac{1 - \Gamma_m e^{2j\beta_t D}}{1 + \Gamma_m e^{2j\beta_t D}}\,, \tag{4.10}$$

where:

$$Y_t = \frac{\sqrt{\epsilon_t}}{60 \ln\left(\frac{b}{a}\right)}, \tag{4.11}$$

- D is the length of the coaxial probe,
- β_t is the propagation constant in the coaxial probe,
- Γ_m is the measured reflection coefficient at the probe connector plane.

Combining the previous equations, complex permittivity is given by the following equation [115]:

$$\bar{\epsilon_r} = \frac{-jc\sqrt{\epsilon_t}}{2\pi f L} \cdot \frac{1 - \Gamma_m e^{2j\beta_t D}}{1 + \Gamma_m e^{2j\beta_t D}} \cdot \cot\left(\frac{2\pi f L\sqrt{\epsilon_d}}{c}\right), \tag{4.12}$$

where:

- D is the physical length of the coaxial probe,
- ϵ_t is the dielectric constant of coaxial cable dielectric,
- c is the wave velocity in free space,
- f is the operating frequency.

The only two unknown variables are D and L, and both are obtained by calibration performed with two well-defined materials.

5. Limitations when measuring with an open-ended coaxial probe

In this chapter, the focus will be on the sources of error and uncertainties in the permittivity measurements done with the OECP. There are a lot of factors that influence the results, such as: measurement errors of the magnitude and phase of the S parameters due to the limited VNA accuracy, agreement between the calibration standards and the actual models representing said standards, setup drift and others that are mostly unpredictable and will vary from setup to setup as covered in [116]. The following subchapters will be dedicated to the uncertainties that can be reasonably quantified such as errors due to the operating **frequency limits**, **heterogeneity of the sample**, measurement of **layered media**, improper **sample contact** with the probe and unsuitable **sample size**.

5.1. Frequency limitations

Even though the coaxial line used for complex permittivity measurements is excited with the TEM wave which has no cutoff frequency, both upper and lower operational frequency limits still exist. **Lower frequency limit** of a probe is present because of the **probe polarization effect** which is a parasitic phenomenon especially apparent when measuring conductive media. Even when the measured sample has negligible conductivity, the low frequency limit still exists because of the insufficient measurement resolution of permittivity at low frequencies. Both inner and outer conductor of a coaxial line behave as a metallic electrode which attracts a surface charge due to the attraction of ions from a conductive sample in which the probe is immersed or pressed against an open end. That first layer of newly formed surface charge attracts oppositely charged ions that cluster around the first layer forming an electrical double layer. In practice, due to electrochemical reactions at the electrode, it is necessary to include a conductance term. The polarization effect thus must be modelled with a complex impedance that includes a capacitor to account for the ion bilayer and additional voltage drop to model the electrochemical reactions [91]. It is possible to reduce the electrode polarization (EP) by several different procedures: variation of the gap between the electrodes, use of four instead of two electrodes, increasing the surface area of the electrode or by coating the electrodes with platinum or other, even less reactive, solutions and thus reduce the surface charge on the electrode. Another alternative is to make the measurements as usual and then remove the artifacts from the results by post processing. One can either subtract the equivalent circuit that models the polarization effects from the measured load impedance or empirically fit the EP data on the appropriate empirical function [117].

Feldman *et al.* [117] have compared three postprocessing EP correction methods they developed for time domain dielectric spectroscopy: the substitution method, the single-exponent method, and fractal method. The first two methods are suitable for both frequency and time domain and they both provide the equivalent circuit for the electrical double layer through linear impedance. The third method, which accounts for the fractal nature of the EP, can only be applied directly in time domain. Out of the three methods, only the substitution method requires an additional measurement of a referent sample that mimics the MUT. Fractal method is suitable for measurements with especially prominent polarization effect such as on highly conductive samples, but it is most sensitive to the design of the sample holder.

Ishai *et al.* [118] have compared the three known methods for suppressing the electrode polarization: analytical modeling of the polarization effect and postprocessing the results, varying the size of the gap between the electrodes, and coating the electrode in a conductive polymer. Their results showed that the analytical technique, modelling the electrode polarization by a parallel RC circuit, is the most reliable. Coating the probe yields a variation

in the input impedance of the probe which is not suitable for consistent measurements. Gap variation has proved successful, but it requires a larger sample which made it less practical than the analytical correction.

Bobowski and Johnson [91] have noted the occurrence of the deviations in the results of the measured liquid solutions due to the electrode polarization effect. The effects were standing out at frequencies under 10 MHz, but the lingering polarization effects, although weaker, were visible even above 300 MHz. The analytical correction was done using the following equivalent circuit for the polarization effects:

$$Z_p = R_p + \frac{1}{j\omega C_p} \tag{5.1}$$

which was subtracted from the measured load impedance. The correction of the real component of the complex permittivity made it a better fit for the expected data, while the polarization had no effect on the imaginary component. This correction is not unconditional as it stops being applicable at frequencies where the polarization impedance Z_p is much larger than the impedance of the aperture and the sample.

High frequency limit coincides with the excitation of **higher order modes** within the coaxial line. Below the limit, the TEM mode is the only propagating mode. In the TEM mode, the electric field lines stretch out radially from the center conductor along the whole coaxial line as shown in Figure 5.1a. except in the vicinity of the probe aperture where the fringing fields occur. First higher order mode to propagate in a coaxial line is the TE_{11} mode (shown in Figure 5.1b) with a cutoff frequency of [91]:

$$f_c \approx \frac{2c}{\sqrt{\epsilon_r}\,\pi\,(D+d)} \tag{5.2}$$

where:

d is the diameter of the center conductor, and

D is the inside diameter of the outer conductor.

Both *d* and *D* are annotated in Figure 5.1. It is evident from the equation that reducing the size of the coaxial probe increases its cutoff frequency.

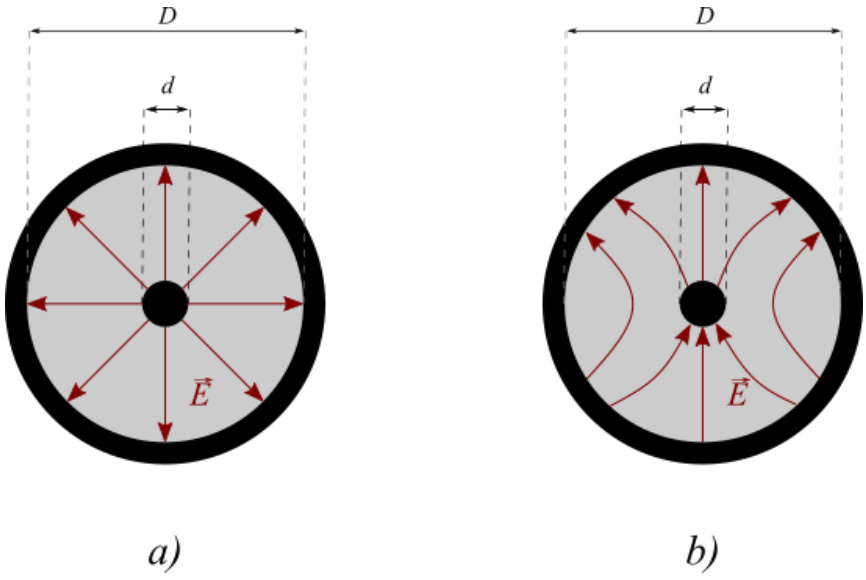

Figure 5.1 Electric field lines in a coaxial cable operating in a) TEM mode b) TE_{11} mode

Upper frequency limits of some of the most common coaxial connectors are shown in Table 5.1.

Table 5.1. Calculated upper frequency limits given for more common types of coaxial connectors.

Type of coaxial connector	d [mm]	D [mm]	ϵ_r	Calculated f_c [GHz]	Recommended maximum operating frequency from the datasheet [GHz]
N	3	7	2.1	13.2	11 [119]
SMA	0.94	4.59	2.1	23.8	18 [120]
3.5 connector	1.52	3.5	1	38	34 [121]
2.4 connector	1.04	2.4	1	55.4	50 [122]

Not accounting for the higher order modes in the calibration models results in the decrease in the accuracy of the model. Additionally, at even higher frequencies, there are **probe radiation effect** that needs to be included in the model as the free-space radiation conductance. Radiation conductance term varies from model to model, but the most common conductance term used is $G_0(\omega)\epsilon_r^{5/2}$ [108]–[110] where $G_0(\omega)$ is the free-space radiation conductance [123]. It correlates to the antenna (radiation) de-embedding model covered in Chapter 4.2.2.

Shibata and Kobayashi [124] have examined the errors that arose when the radiation resistance was not included in the equivalent model. The study was done on a flanged probe using the MoM for three frequencies: 0.5, 1.5 and 3 GHz. Flange diameter was 30 mm, while center conductor had a diameter of 1.3 mm, and the inner diameter of an outer conductor was 4.1 mm. Results showed that the percentage error at 3 GHz was larger than for the lower two frequencies which was expected as the radiation increases with frequency.

5.2. Heterogeneous media

5.2.1. Uniform heterogeneity

Dielectric properties of a uniformly heterogeneous or composite medium depend on the properties and proportions of its constituents. It is in itself difficult to determine the dielectric properties of a heterogeneous medium, even with known constituents. Moreover, measuring said properties with an OECP creates additional complications and dilemmas. Is the taken sample an accurate representation of the heterogeneity of the medium? Is the sample size too small to make accurate measurements, or perhaps even too large for a single point measurement? If so, is it necessary to measure the sample at several different points and average them? How many points should be measured? How should the average be weighted? Those are only some of the questions that should be answered before even starting the measurement to ensure that the methods are adequate.

Estimation of the effective complex permittivity of the mixture ϵ_{eff} made up of particles of the solid material dispersed in a host medium is done by dielectric mixture equations. It is necessary to know the dielectric properties of the host medium and the inclusions ϵ_i, and their corresponding volume fractions v_i (i = 1, 2, …, N). No matter the number of inclusions i, the sum of the volume fractions must equal to one. There are several variations of the equations with one of the most notable one being the Complex Refractive Index Model (CRIM) [125]:

$$\epsilon_{eff}^{\frac{1}{2}} = \sum_{i=1}^{N} v_i \epsilon_i^{\frac{1}{2}} . \tag{5.3}$$

It is an empirical model most commonly used for soils and concrete materials. CRIM model is derived from the Power-Law model, just like the Landau and Liftshitz, Looyenga (LLL) mixture model [126] is derived by adjusting the exponent value to 1/3:

$$\epsilon_{eff}^{\frac{1}{3}} = \sum_{i=1}^{N} v_i \epsilon_i^{\frac{1}{3}} \ . \tag{5.4}$$

There is also the Lichtenecker equation which uses logarithmic functions [18]:

$$\log \epsilon_{eff} = \sum_{i=1}^{N} v_i \log \epsilon_i \ . \tag{5.X}$$

Another famous mixture model is the Bruggeman symmetric model [127]:

$$\sum_{i=1}^{N} v_i \frac{\epsilon_i - \epsilon_{eff}}{\epsilon_i + 2\,\epsilon_{eff}} = 0 \, . \tag{5.5}$$

The model maximizes the interactions between inclusions which is contrasting to the Maxwell Garnett model [128] that minimizes the interaction between inclusions:

$$\epsilon_{eff} = \epsilon_h + 3\epsilon_h \frac{\sum_{i=1}^{N} f_i \frac{\epsilon_i - \epsilon_h}{\epsilon_i + 2\epsilon_h}}{1 - \sum_{i=1}^{N} f_i \frac{\epsilon_i - \epsilon_h}{\epsilon_i + 2\epsilon_h}}, \tag{5.6}$$

where ϵ_h is the host complex permittivity which must be discerned from the inclusions. That differentiates it from the models in Eq.5.3 – 5.5 where it was not necessary to discern between the host and the inclusions. It is imperative for the inclusions to be spheric and isotropic, and that the volume fraction of the host is much larger than of the inclusions. The equation is not applicable when the volume fractions of all components are comparable. It is suitable for mediums made of inclusions randomly spread in a matrix.

Over the years, there were numerous studies that compared the permittivity obtained theoretically with the mixture equation calculation and the permittivity obtained experimentally by the OECP measurements. Most of the work done was on pulverized materials as it is more suitable for the OECP technique than the solid material. Nelson and Bartley [126] have attempted to characterize pulverized coal and limestone at 51 frequency points from 0.2 to 20 GHz with the OECP and compare it to the LLL dielectric mixture equation (Eq. 5.4). The results showed reasonable match between the two fitted permittivities. The main source of uncertainty laid in the dielectric loss factor measurements as the OECP method did not give accurate results for such low loss materials because of the reflections from the dielectric interfaces. Baharudin *et al.* [129] have tried to characterize pulverized agricultural waste for the microwave absorber applications. Their measurements have been carried out in the 10 – 20 GHz range. They have also used the LLL mixture model (Eq. 5.4). Permittivity results acquired with the OECP had consistently lower values of the real component than the theoretical values for each of the three materials tested. They hypothesized that it was due to the underestimation of the air constituent that additionally filled up the gap in the pulverized material.

Van Damme *et al.* [19] have measured the permittivity of the hardened concrete slabs that are reinforced with steel fibers. The effective permittivity of the heterogeneous slab was derived from several spaced-out local measurements with an averaging procedure. A Maxwell–Garnett type of analytical relation between the effective permittivity and the fiber volume fraction has been derived (Eq. 5.6). Although the effective permittivity could be measured with a larger aperture probe without the complications of the additional averaging and calculations, the advantage of the employed process is that it eliminates the need for a larger sample or a more complex de-embedding model that would account for the finite thickness of the layer that would be sensed by a larger probe. Guihard *et al.* [125] have tested the results obtained with three different mixture models: Maxwell Garnett (Eq. 5.6), Bruggeman (Eq. 5.5) and CRIM model (Eq. 5.3). Test sample was a material made of spherical inclusions with $\epsilon_i = 4.6$ embedded into a matrix having a permittivity equal to 1 i.e., dry sand with air. The working frequency range was from 1 MHz to 4 GHz. They have compared the experimental measured results with the results obtained using Finite Element Method (FEM) simulations with fabricated materials having a permittivity equal to the calculated results from different mixing equations. Their results showed that the Bruggeman model (Eq. 5.5) was the most accurate one as it was expected because it is the most appropriate for mixtures with high volume fraction of inclusions.

The mixing equations can also be used on the biological cells suspended in a culture medium. Odelstad *et al.* [130] have measured complex permittivity of cell suspensions made from different cell lines such as bone and muscle cells of varying concentrations in a suspension medium. They have used a variation of the Maxwell Garnett model to calculate the permittivity of the cells from the difference in the permittivity between the cell suspensions and pure culture medium. Lodi *et al.* [18] have even investigated the validity of several mixing formulas for predicting the permittivity of the bread dough mixture. The used models were Maxwell Garnett model, Bruggeman model, Lichtenecker model and several Power-Law models. Comparison with OECP measurements from 0.5 to 9.5 GHz showed that the Power-Law model was the best at modelling the actual dough permittivity in the range from about 2.45 GHz to 8.5 GHz.

5.2.2. Layered Media

Similar to the heterogeneous media, layered media produces permittivity results as a combination of dielectric parameters of all layers. However, unlike the issue of uniform heterogeneity, the success of the measurement of layered media is mostly dependent upon the sensing depth of the probe. Chen *et al.* [131] presented a de-embedding model of an OECP measuring bilayered dielectric sample. It is a variation of the capacitive model covered in Chapter 4.2.1., but with an added parallel capacitance arising from the second layer as shown in Figure 5.2. The measurements were made in the 0.6 - 2.6 GHz spectrum on the different saline solutions under a wax slice or scotch tape. Permittivity of the either layer was adequately calculated even without the knowledge of the thickness of the first layer.

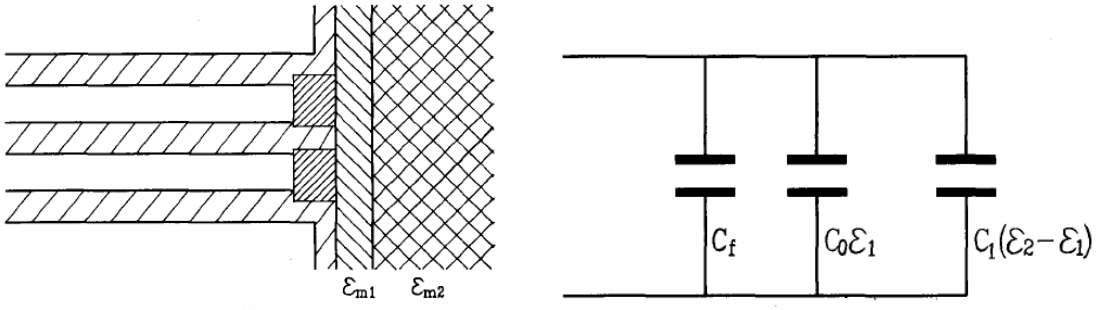

Figure 5.2. OECP pressed against layered media (left) and an equivalent circuit for that setup (right) [131]

One year later, Li and Chen [132] have provided a full wave analysis of the flanged OECP placed against a layered MUT over a 0.3 – 4 GHz frequency range. Accuracy was generally sufficient, with the exception of instabilities for low-permittivity materials at frequencies under 1 GHz. Aydinalp *et al.* [133] have tested a two-layer skin and PEC (perfect electric conductor) bilayered structures using CST Microwave Studio software. Simulations were done from 500 MHz to 2 GHz on probes of three different aperture diameters: 0.5 mm, 0.9 mm, and 2.2 mm with variable skin thicknesses. They have concluded that the minimum skin thickness needed to achieve results that fit the homogeneous sample is 0.9 mm, 1 mm, and 2 mm for probe apertures of 0.5 mm, 0.9 mm, and 2.2 mm respectively.

Although the authors in [134] referred to their sample setup as an example of tissue heterogeneity, the setup consisted of two horizontal layers of five contrasting material pairs such as duck fat and porcine muscle, deionized water and acrylic, etc. Lower layer was a solid MUT fixated to the bottom of the beaker, while the upper layer was liquid MUT in which the probe was immersed. Thickness of the upper layer was controlled by the variation in the immersion of the probe. They have attempted to relate the permittivity contribution of the tissue with its thickness, but the results showed that no such association could be made because it varies widely depending on the layer materials and any simplification would introduce large errors. La Gioia *et al.* [135] have tested the effect of radial heterogeneities using rubber-based phantoms composed of two side by side materials in a measurement setup as shown in Figure 5.3. They have demonstrated that the measured permittivity is an average of the permittivities of the two constituents. Furthermore, they made evident how the probe sensing depth or, as they named it, histology depth, increases with the increasing permittivity of the material below the probe and is midway between the histology depths of the constituent materials.

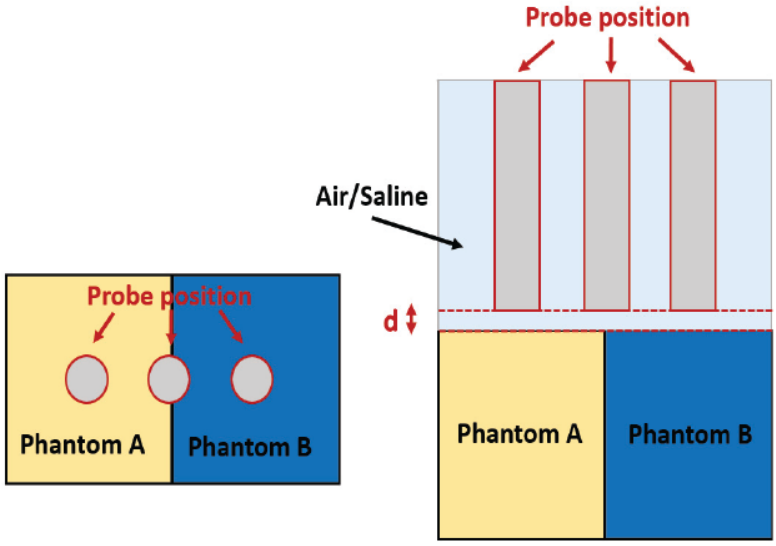

Figure 5.3. OECP measurement setup for measuring radial heterogeneities from [135]. *Top view of the setup is shown on the left, while a side view is displayed on the right. Variable thickness of the first layer d is also marked in the side view.*

In 2014, Meaney *et al.* [136] have tested the sensing volume of the OECP by measuring a two-layer composition consisting of a liquid as a top layer and a Teflon cylinder as the bottom layer as shown in Figure 5.3. The probe used for measurements and modelled in a simulation was Keysight's Slim Form Probe. The measurements were done from 0.5 to 8.5 GHz with 100 MHz increments while the simulations were done at 2 GHz. They used two different liquids: deionized water and 0.9% physiological saline. Teflon was moved at several exact distances

from the probe, allowing for the liquid to fill the interspace. As the Teflon was kept in contact with the probe, the measured permittivity matched the permittivity of Teflon. Distancing the Teflon from the probe tip resulted in a drastic change in the measured permittivity in the favor of liquid. As the Teflon was distanced at only 0.2 mm from the probe, the measured permittivity was an average value of both Teflon and intervening liquid, while at the distance of 0.5 mm from the probe tip, resulting permittivity was 90% of the liquid. The results implied that the probe's sensing depth is much shallower than previously assumed. Two years later, using the same experimental setup, Meaney *et al.* [137] have characterized the effective penetration depth of a probe as the distance when the measured relative permittivity at that separation distance drops 20% below that of the straight line extrapolated from the straightest section of the curve beginning at exact contact of the lower sample with the probe. Example of the effective penetration depth calculation is shown in Figure 5.3. Measured and simulated results at 300 MHz for two different probes, Delfin models D15 and M25 showed the consistency in effective penetration depth between measurements and simulations and a clear dependence on the probe diameter. In other simulation study, the penetration depth for a fixed probe geometry that corresponded to the RG-402 coaxial cable did not vary considerably from 0.5 to 10 GHz with only a slight increasing trend at the higher frequencies.

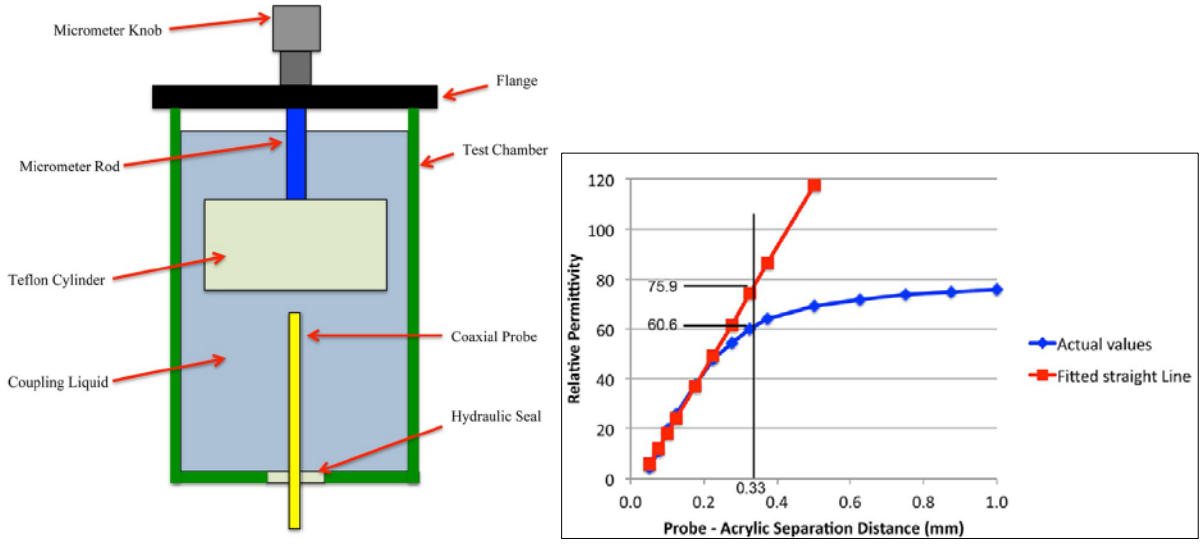

Figure 5.3. Experimental OECP test configuration for the sensing depth investigation done in [136] *(left). Example of a calculation of the effective penetration depth from* [137] *(right).*

In 2019, Šarolić [138] recreated and confirmed the conclusions of Meaney's study that the OECP is very limited in terms of sensing the layers below the one that is in contact with the probe, even when the first layer is thin i.e. a few tenths of a millimeter for a coaxial probe based on the RG405 coaxial cable geometry. The computational study was done at 2 GHz on two different model setups. The first setup consisted of water-Teflon combination similarly to the setup shown in Fig. 5.3., while the other represented the biological layered tissue consisting of skin, fat, and muscle. Subsequent simulation study [139] examined the impact of the upscaling of the probe up to five times on the sensing of the deeper layers. Layered models were kept the same as in the previous study. Although the upscaled probes had greater penetration of the electric field into the MUT, the measured permittivity was still dominantly influenced by the surface layer of the MUT.

5.3. Sample contact

Air gaps in solids, usually analyzed as a layered capacitor, can be a significant source of error. The surface roughness of the sample traps air gaps when pressed against a flat probe aperture surface. Uneven MUT surface is even more noticeable if the measuring OECP has a flange. **Lift-off** is another term found in the literature for the air gap between the probe and the sample. Baker-Javis *et al.* [140] have first carried out a full-wave analysis of an OECP with lift-off for three cases: infinite sample, sample backed by a well-characterized material, and sample backed by a short circuit. Numerical results showed the large extent of probe's sensitivity to air gap. To mitigate the unwanted sensitivity, larger probes or higher frequencies should be used. Reader and Janezic [141] have examined the issue of lift-off experimentally with two samples, one having a low permittivity value of 5, and the other with a higher relative permittivity of 50. Both materials showed decreasing permittivity values as the air gap got larger, while the measured frequency had virtually no effect on the results. Fallahi *et al.* [104] have presented a difference in the real and imaginary part of complex permittivity for a 2-mm thick sample without an air gap and with a 2 μm air gap. Although the difference was not substantial for the sample having $\epsilon_r = 2$, the difference was indeed noticeable for sample with $\epsilon_r = 30$, which led them to the calibration protocol which includes effective air gap calculation. The goal was to keep the measurements of thin samples as accurate as possible even when the probe surface is rough while presuming that the measured sample has a negligible surface roughness. Air gaps due to the surface roughness are mostly considered and quantified when the samples are particularly thin, as in [142] and [143].

Similar issue arises when there is no adequate **contact pressure** applied over the sample. Numerous sources in the literature have pointed at the faulty contact with the sample as the source of measurement uncertainty due to the variations in the pressure applied [144]–[146]. In most cases they mention that the insufficient pressure allows for air gaps [147], while the excess pressure can crush the structure of a sample [148]. Ideally, one could use a pressure gauge or sensor if the measurement setup allows so as done in [149], [150] to control for a steady pressure and as a result have a more repeatable measurement. In [151], the authors reported using a digital scale to keep the pressure stable. Mehta *et al.* [152] have investigated the influence of different measurement parameters on the measured dielectric properties of skin, giving special attention to the amount of pressure exerted on the sample. Although the pressure was not quantified, they have specified using three different applied pressures. It is important to note that all pressure variations included a full probe contact with the skin. The measured values of reflection coefficient magnitude were within 3% of one another as shown in Figure 5.4. The results imply that when the proper contact is ensured, there should not be a large variation in results for different pressures when measuring skin on human subjects.

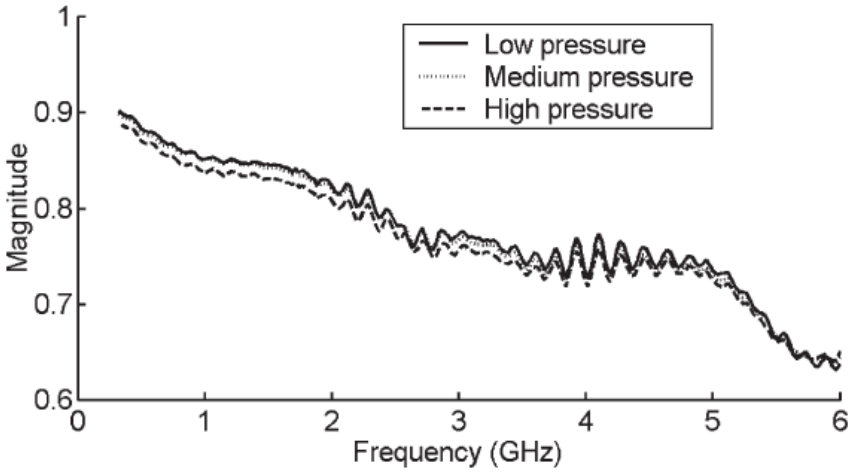

Figure 5.4. Measured magnitude of the reflection coefficient as a function of frequency for three different applied pressures [152]

Shrestha *et al.* [148] have also recognized the importance of optimal pressure for their measurements on alfalfa leaves. At lower pressures, the dielectric constant increased with pressure, while at higher pressures there was a point where the pressure increased rapidly which was attributed to the sample destruction. In 2020, Maenhout *et al.* [153] have done a comprehensive research on the effects of probe-to-tissue contact pressure when performing dielectric measurements on biological tissues i.e. bovine liver in their instance. During the pilot measurements, there was an exponential decaying pressure over time as the liver tissue conformed to the shape of the probe as shown in the Figure 5.5. The solution included a lifting platform that compensated for the pressure decay and kept the pressure relatively constant. That allowed them to test 10 different pressure levels varying from 7.74 kPa to 77.4 kPa. They have concluded that the application of varying pressures changed the cellular matrix of the tissue and resulted in an average relative change of -0.31 and -0.32 for the real and imaginary part of complex permittivity per kPa, respectively. The variations and the specificities of the optimal pressure value in all of the aforementioned studies implies that there should be a material-specific approach when it comes to choosing the most favorable contact pressure depending on the sample type.

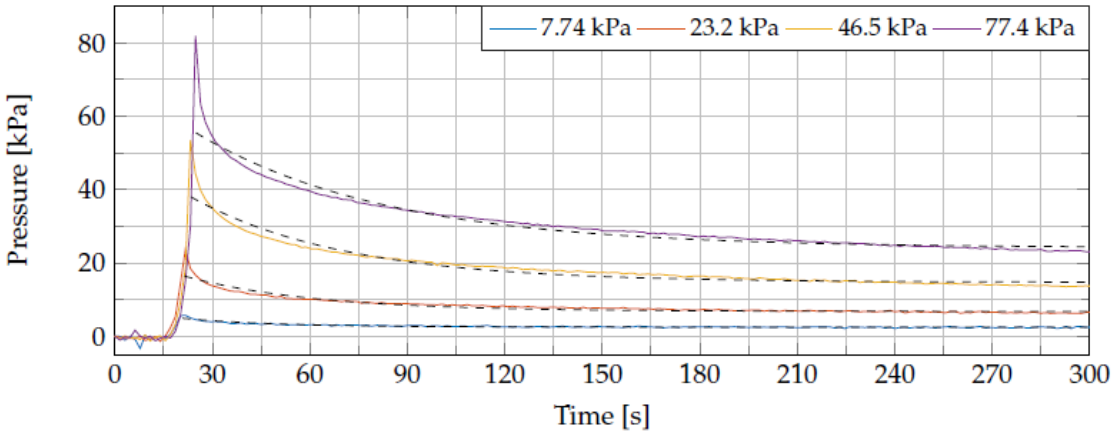

Figure 5.5. The exponential decaying pressure behavior due to the tissue conformation around the probe tip for four different applied pressures: 7.74 kPa, 23.2 kPa, 46.5 kPa, and 77.4 kPa [153]

Analogous to the air gaps in solids, **air bubbles** in liquids that stick to the open end of the probe also cause unwanted errors. Odelstad *et al.* [130] have explicitly mentioned in their work that one of the reasons for high measurement uncertainty was the formation of air bubbles on the tip of the probe. Bubbles were visually observed on at least one occasion. The bubbles were forming either during the calibration process, which resulted in corrupt calibration, or during the calibration validation or the actual measurements. The procedure after bubble formation included wiping the probe tip with a paper towel and redoing the measurement and calibration if necessary. The issue becomes more common when measuring liquids at higher temperatures due to the dissolved gasses in the water such as in [154] and [155]. Generally, to the authors knowledge, there is no reported protocol for reducing air bubbles other than their mechanical removal [156].

5.4. Sample size

Most of the de-embedding models are based on the premise that the MUT is infinite in size. As the real-life MUTs are finite in size, the compromise is to agree on an acceptable error due to the finite MUT for the specific measurement case. With the acceptable errors defined, each probe manufacturer provides guidelines on the minimum volume requirement of the sample to ensure that the set error limits are not overstepped. The important remark is that the reflections from the boundaries of the sample that reflect back to the open aperture must be sufficiently small as to not influence the measurement results. That is why the volume restrictions for lossy samples are more lenient in general.

Measurements done on isopropanol up to 125 GHz showed that the results did vary with probe position in the container with isopropanol. Measurement points and the results are shown in Figure 5.6. When the distance from the bottom of the container was at least ca. 3 mm, permittivity results showed good consistency, while some variation was visible with the probe distanced around 1 mm from the container bottom. The variations were less apparent at higher frequencies [95].

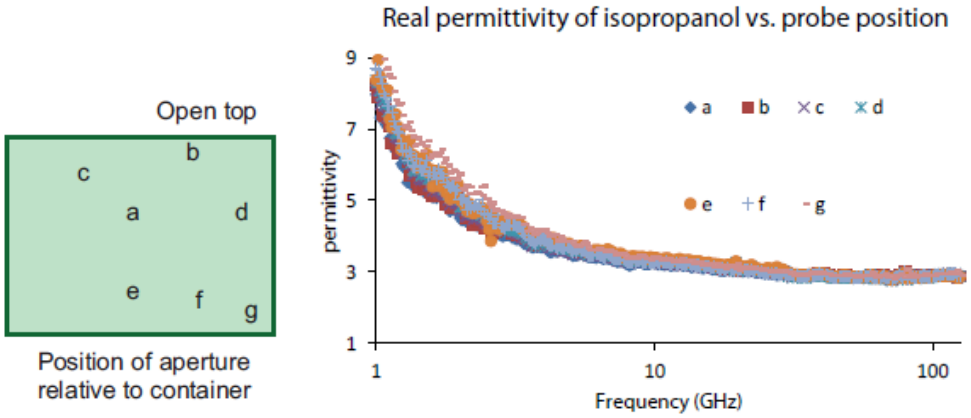

Figure 5.6. Position of the measurement point in the container (left) and the associated real part of the permittivity as a function of frequency (right) [95]

In 2003, Hagl *et al.* [156] have tested, both computationally and experimentally, the sensing volume of a OECP for two probe diameters: 2.2 and 3.58 mm. Setup for determining the radial and axial boundary is shown in Figure 5.7. Measured samples were standard calibration liquids: methanol, ethanol and deionized water, whose permittivity corresponded to both high, intermediate, and low-water content tissues. Sensing was determined by identifying the smallest distance of the probe from the bottom or the edge of the beaker for which the errors stay below the threshold of 1.5% for magnitude and 2.5° for the phase of S_{11}. Those exact values

of error were chosen as they produce a 10% error in the real and imaginary part of the complex permittivity, a value that is considered as the acceptable level of error by the authors. Their data showed that the minimum tissue specimen for accurate results had 3 mm thickness and 1.1 cm width for larger probe, and 1.5 mm thickness and 5 mm width for narrower probe. Although their objective was breast tissue characterization, the results are also relevant for other biological tissues. Their findings were additionally experimentally confirmed by pork belly measurements done in [157] where the authors showed that the sensing region is not much larger than the probe tip. It also validated the groups previous results on radial heterogeneities [135].

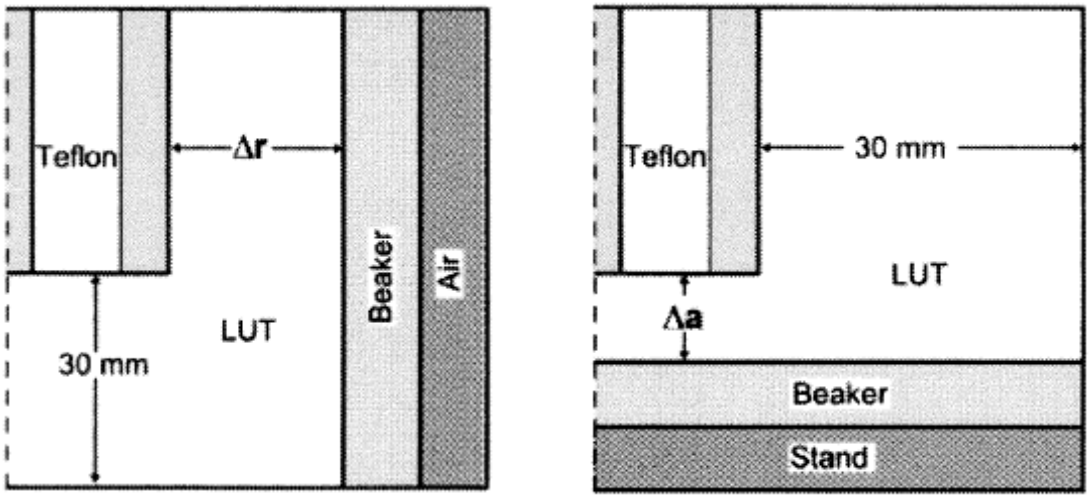

Figure 5.7. OECP setup for investigating the influence of radial boundary (left) and axial boundary (right) from [156]

La Gioia's group has done extensive research on the topic of sensing volume of the OECP, and their results indicated that:

- The sensing radius increases with the contrast in permittivity between the constituent tissues. Sensing radius was calculated as a radius at which the outer radial sample does not influence the permittivity results. The uncertainty limit was set at 2.5% as it was the measurement uncertainty of 0.1 M NaCl solution observed in experiments [158].
- The sensing radius is highly dependent on the permittivity of the tissue closest to the inner conductor of the probe. For the samples consisting of two concentric tissues, the higher sensing radius is detected when the inner tissue has a higher permittivity i.e. muscle as the inner sample provides a higher sensing radius than having the fat as the inner sample [158].
- The histology radius does not exceed the probe radius which was 1.1 mm in their experiments. They measured saline samples surrounded by Teflon walls at five different frequencies: 0.5 GHz, 4 GHz, 8 GHz, 14 GHz and 20 GHz and obtained highly repeatable results. Their findings were confirmed on porcine tissue measurements as the muscle and fat tissues surrounding the probe did not affect the dielectric measurements of the sample underneath the probe [159].
- The dielectric properties of radially heterogeneous tissues depend on the spatial distribution of each material within the histology radius and not on the percent volume occupied [159].

- The bulk dielectric properties of concentric heterogeneous tissues highly depend on the properties of each constituent material within the histology radius. If the inner material has low permittivity, it has approximately 50% higher impact on the measured total permittivity of the sample than the outer material, whereas if it has high permittivity, the contribution of both materials is proportional to the percent volume occupied in the sample [159].
- The dielectric contribution of a particular tissue depends on both its location within the sensing volume and its dielectric properties. Side-by-side tissues contribute equally [160].
- That there is a nonlinear relationship is found between the contribution of individual tissues to the acquired dielectric data and the volume that each tissue occupies within the radially heterogeneous sample. The weighted contribution was modelled using the generalized logistic function for inner tissue:

$$w_{T1} = \frac{1}{(a + be^{-cr})^{\frac{1}{d}}}, \tag{5.7}$$

and

$$w_{T2} = 1 - \frac{1}{(a + be^{-cr})^{\frac{1}{d}}}, \tag{5.8}$$

for the outer tissue. The r is the radius of the inner tissue, while a, b, c, and d are the parameters chosen as the best fit with the smallest root-mean-square-error for each tested inner and outer tissue combination [161].

- The sensing radius is greater when a high permittivity tissue is in contact with the probe tip as confirmed by the numerical simulations on concentrically arranged tissue samples consisting of fat and gland tissues. The largest sensing radius obtained was 1.45 mm for a probe having a 1.1 mm outer radius. The uncertainty limit that, in turn, defined the sensing radius was experimentally observed to be 2.1% for relative permittivity and 4.2% for conductivity [162].
- The trends of the sensing radius increase with the probe dimensions are consistent across different samples as experimentally tested on three commercial Keysight probes: slim form, performance, and high temperature probe [163].
- Additional simulations were modelled to test a variety of probe dimensions. Probe outer diameter was fixed at 1 mm as was shown that the sensing radius is not affected by the width of the outer conductor [163].
- The inner conductor width has the largest impact on the sensing radius where the sensing radius increases linearly with the inner conductor radius [163].

Latest numerical simulation analysis on the topic of sensing volume done by Farshkaran and Porter [164] showed that the usual cylindrical representation with the depth and radius of the sensing volume of the OECP probe may not be an ideal representation. Simulated probe had an outer diameter of 2.2 mm, while the inner conductor had a diameter of 0.5 mm. Probe was 40 mm long. They modelled the probe using the finite element method which provided them with a full-wave solution. After observing the electrical field isosurfaces in the vicinity of the probe and sensing depth and radius, they concluded that the elliptical shape should be considered instead. The proposed ellipsoidal sensing volume was further tested with four sample shapes that included two cube and two sphere volumes included in a homogenous background which confirmed their observations.

6. Conclusion

This work compiles the most widely used measurement methods in the microwave frequency range. The methods are separated into three groups: reflection methods, resonant methods, and transmission/reflection methods. Reflection methods include all of the methods where the permittivity is extracted from the reflection due to the impedance mismatch at the location of the inserted measured material. Resonant methods cover the measurement techniques that calculate the permittivity from the quality factor and the resonant frequency of the resonator which inevitably makes the measurements narrowband. Last group includes the setups where the permittivity is extracted from both transmission and reflection coefficients.

The focus of the second half of the work is kept on the open-ended coaxial probe (OECP) as the method that falls under the reflection methods. The OECP method is thoroughly covered in the literature as the sample preparation is simple and typically nondestructive while it generally gives reasonably accurate results in a broad frequency range. The coaxial probe with its open end is pressed against the sample (i.e. material under test - MUT) and excited with a TEM wave. Said wave reflects from the MUT, with the complex permittivity of the MUT embedded in the complex reflection coefficient, which is measured by a vector network analyzer (VNA). De-embedding can be achieved by modeling the probe open end terminated by MUT using equivalent circuits and models. Here, four different de-embedding models were described: capacitive model, antenna model, rational function model, and virtual transmission line model. No matter the model used, the accuracy of the permittivity measurement is primarily based on the proper calibration that aims to cancel out the systematic errors of the measurement setup. To date there are several different commercial dielectric measurement kits with different probe types suitable for various measurements, which attests to the applicability of the method.

Current unresolved limitations of the method include, among other, lower and upper frequency limits. Lower frequency limit is present because of the probe polarization effect, which introduces significant inaccuracies. Upper frequency limit is defined with the set probe geometry and exceeding that limit implies the inclusion of unaccounted higher order modes in the measurement results. One of the largest disputes around the OECP method is defining its sensing volume. Although many studies have been done that attempted to characterize the exact sensing volume, there is still no consensus on what that volume is for a probe with set geometry. Lack of knowledge on the exact sensing volume leads to further limitations and uncertainties when measuring small samples, uniformly heterogeneous materials, layered materials, thin samples, etc.

To recapitulate, even though the modern open-ended coaxial probe measurement technique encompasses decades of improvements and refinements, there is, nevertheless, the need for further improvements. The major issues to be resolved are: to further widen the operating frequency range, to improve the measurement accuracy by the adequate selection of de-embedding models and measurement procedures, and to improve the dielectric characterization of various types of inhomogeneous samples.

References

[1] B. Riddle, J. Baker-Jarvis, and J. Krupka, “Complex permittivity measurements of common plastics over variable temperatures,” *IEEE Trans. Microwave Theory Techn.*, vol. 51, no. 3, pp. 727–733, Mar. 2003, doi: 10.1109/TMTT.2003.808730.

[2] Z. Abbas, You Kok Yeow, A. H. Shaari, K. Khalid, J. Hassan, and E. Saion, “Complex permittivity and moisture measurements of oil palm fruits using an open-ended coaxial sensor,” *IEEE Sensors J.*, vol. 5, no. 6, pp. 1281–1287, Dec. 2005, doi: 10.1109/JSEN.2005.859249.

[3] Z. Abbasi, H. Niazi, M. Abdolrazzaghi, W. Chen, and M. Daneshmand, “Monitoring pH Level Using High-Resolution Microwave Sensor for Mitigation of Stress Corrosion Cracking in Steel Pipelines,” *IEEE Sensors J.*, vol. 20, no. 13, pp. 7033–7043, Jul. 2020, doi: 10.1109/JSEN.2020.2978086.

[4] J. H. Kang, S. Park, and S. Cho, “A Relative Permittivity-Based Air Pressure Sensor Using Standard CMOS Process,” *IEEE Sensors J.*, vol. 17, no. 12, pp. 3892–3899, Jun. 2017, doi: 10.1109/JSEN.2017.2695124.

[5] R. N. Dean, J. D. Craven, E. A. Guertal, and K. A. Varnavas, “A PCB Sensor for Status Monitoring of Stored Food Stocks,” *IEEE Sens. Lett.*, vol. 3, no. 4, pp. 1–4, Apr. 2019, doi: 10.1109/LSENS.2019.2902837.

[6] N. R. Peplinski, F. T. Ulaby, and M. C. Dobson, “Dielectric properties of soils in the 0.3-1.3-GHz range,” *IEEE Trans. Geosci. Remote Sensing*, vol. 33, no. 3, pp. 803–807, May 1995, doi: 10.1109/36.387598.

[7] B. Matthieu, R. Jerome, B. Stephane, and L. Gabriel, “Evolution of the complex permittivity of biological tissue at microwaves ranges: Correlation study with burn depth,” in *2014 36th Annual International Conference of the IEEE Engineering in Medicine and Biology Society*, Chicago, IL, Aug. 2014, pp. 4054–4057. doi: 10.1109/EMBC.2014.6944514.

[8] M. E. Martín-Esparza, N. Martínez-Navarrete, A. Chiralt, and P. Fito, “Dielectric behavior of apple (var. Granny Smith) at different moisture contents,” *Journal of Food Engineering*, vol. 77, no. 1, pp. 51–56, Nov. 2006, doi: 10.1016/j.jfoodeng.2005.06.018.

[9] Y. Wang, L. Zhang, M. Gao, J. Tang, and S. Wang, “Temperature- and Moisture-Dependent Dielectric Properties of Macadamia Nut Kernels,” *Food Bioprocess Technol*, vol. 6, no. 8, pp. 2165–2176, Aug. 2013, doi: 10.1007/s11947-012-0898-2.

[10] M. M. Isa, N. Ibrahim, R. Shamsudin, and M. H. Marhaban, “Sugar content in watermelon juice based on dielectric properties at 10.45GHz,” in *2009 IEEE Student Conference on Research and Development (SCOReD)*, UPM Serdang, Malaysia, 2009, pp. 529–532. doi: 10.1109/SCORED.2009.5442945.

[11] A. Reyes, M. Yarleque, W. Castro, and S. Chuquizuta, “Determination of dielectric properties of the red delicious apple and its correlation with quality parameters,” in *2017 Progress in Electromagnetics Research Symposium - Fall (PIERS - FALL)*, Singapore, Nov. 2017, pp. 2067–2072. doi: 10.1109/PIERS-FALL.2017.8293478.

[12] H. T. Shivamurthy, I. Matacena, and M. Spirito, “Dielectric measurements of mangoes from 0.5GHz to 20GHz using a custom open-ended coaxial probe,” in *2017 47th European Microwave Conference (EuMC)*, Nuremberg, Oct. 2017, pp. 958–961. doi: 10.23919/EuMC.2017.8231005.

[13] W. Guo, “Dielectric properties of honey adulterated with sucrose syrup,” *Journal of Food Engineering*, p. 7, 2011.

[14] S. Clerjon and J.-L. Damez, “Microwave sensing for an objective evaluation of meat ageing,” *Journal of Food Engineering*, vol. 94, no. 3–4, pp. 379–389, Oct. 2009, doi: 10.1016/j.jfoodeng.2009.04.004.
[15] L. Ragni, A. Al-Shami, G. Mikhaylenko, and J. Tang, “Dielectric characterization of hen eggs during storage,” *Journal of Food Engineering*, vol. 82, no. 4, pp. 450–459, Oct. 2007, doi: 10.1016/j.jfoodeng.2007.02.063.
[16] M. Castro-Giráldez, P. J. Fito, and P. Fito, “Application of microwaves dielectric spectroscopy for controlling pork meat (Longissimus dorsi) salting process,” *Journal of Food Engineering*, vol. 97, no. 4, pp. 484–490, Apr. 2010, doi: 10.1016/j.jfoodeng.2009.11.005.
[17] T. Odedeyi *et al.*, “A Low-Cost Instrument for Estimating the Starch Content of Cassava Roots Based on the Measurement of RF Return Loss,” in *2020 IEEE International Symposium on Circuits and Systems (ISCAS)*, Seville, Spain, Oct. 2020, pp. 1–5. doi: 10.1109/ISCAS45731.2020.9181286.
[18] M. B. Lodi *et al.*, “Microwave Characterization and Modeling of the Carasau Bread Doughs During Leavening,” *IEEE Access*, vol. 9, pp. 159833–159847, 2021, doi: 10.1109/ACCESS.2021.3131207.
[19] S. Van Damme, A. Franchois, D. De Zutter, and L. Taerwe, “Nondestructive determination of the steel fiber content in concrete slabs with an open-ended coaxial probe,” *IEEE Trans. Geosci. Remote Sensing*, vol. 42, no. 11, pp. 2511–2521, Nov. 2004, doi: 10.1109/TGRS.2004.837332.
[20] J. O. Twumasi and T. Yu, “Corrosion current level estimation of rust samples using inverse dielectric spectroscopy,” in *2017 IEEE Electrical Insulation Conference (EIC)*, Baltimore, MD, USA, Jun. 2017, pp. 404–407. doi: 10.1109/EIC.2017.8004648.
[21] S. Hilgedick, J. N. Vutukury, and K. M. Donnell, “Application of open-ended coaxial probes for detection of sand production from petroleum wells,” in *2014 IEEE International Instrumentation and Measurement Technology Conference (I2MTC) Proceedings*, Montevideo, Uruguay, May 2014, pp. 675–680. doi: 10.1109/I2MTC.2014.6860828.
[22] L. P. Gradinarsky, H. Brage, B. Lagerholm, I. N. Bjorn, and S. Folestad, “In-situ Monitoring of Moisture Content in Powder Processing Using Dielectric Probe Measurements with Multivariate Calibration,” in *2006 IEEE Instrumentation and Measurement Technology Conference Proceedings*, Sorrento, Apr. 2006, pp. 308–311. doi: 10.1109/IMTC.2006.328434.
[23] A. H. Abdelgwad and T. M. Said, “Measured Dielectric Permittivity of Contaminated Sandy Soil at Microwave Frequency,” *J. Microw. Optoelectron. Electromagn. Appl.*, vol. 15, no. 2, pp. 115–122, Jun. 2016, doi: 10.1590/2179-10742016v15i2591.
[24] H. Kabir *et al.*, “Measurement and modelling of soil dielectric properties as a function of soil class and moisture content,” *Journal of Microwave Power and Electromagnetic Energy*, vol. 54, no. 1, pp. 3–18, Jan. 2020, doi: 10.1080/08327823.2020.1714103.
[25] B. Velázquez-Martí, C. Gracia-López, and P. J. Plaza-Gonzalez, “Determination of Dielectric Properties of Agricultural Soil,” *Biosystems Engineering*, vol. 91, no. 1, pp. 119–125, May 2005, doi: 10.1016/j.biosystemseng.2005.02.004.
[26] C. Rossmanna and D. Haemmerich, “Review of Temperature Dependence of Thermal Properties, Dielectric Properties, and Perfusion of Biological Tissues at Hyperthermic and Ablation Temperatures,” *Crit Rev Biomed Eng*, vol. 42, no. 6, pp. 467–492, 2014, doi: 10.1615/CritRevBiomedEng.2015012486.
[27] D. Kurrant, A. Baran, J. LoVetri, and E. Fear, “Integrating prior information into microwave tomography Part 1: Impact of detail on image quality,” *Med. Phys.*, vol. 44, no. 12, pp. 6461–6481, Dec. 2017, doi: 10.1002/mp.12585.

[28] D. Kurrant, E. Fear, A. Baran, and J. LoVetri, “Integrating prior information into microwave tomography part 2: Impact of errors in prior information on microwave tomography image quality,” *Med. Phys.*, vol. 44, no. 12, pp. 6482–6503, Dec. 2017, doi: 10.1002/mp.12584.
[29] V. Raicu and Y. Feldman, Eds., *Dielectric relaxation in biological systems: physical principles, methods, and applications*, First edition. Oxford, United Kingdom: Oxford University Press, 2015.
[30] Keysight Technologies, Inc., “Basics of Measuring the Dielectric Properties of Materials,” USA, Application Note, Mar. 2017.
[31] K.-C. Kao, *Dielectric phenomena in solids: with emphasis on physical concepts of electronic processes*. Amsterdam ; Boston: Academic Press, 2004.
[32] K. S. Cole and R. H. Cole, “Dispersion and Absorption in Dielectrics I. Alternating Current Characteristics,” *The Journal of Chemical Physics*, vol. 9, no. 4, pp. 341–351, Apr. 1941, doi: 10.1063/1.1750906.
[33] D. W. Davidson and R. H. Cole, “Dielectric Relaxation in Glycerol, Propylene Glycol, and n-Propanol,” *The Journal of Chemical Physics*, vol. 19, no. 12, pp. 1484–1490, Dec. 1951, doi: 10.1063/1.1748105.
[34] S. Havriliak and S. Negami, “A complex plane representation of dielectric and mechanical relaxation processes in some polymers,” *Polymer*, vol. 8, pp. 161–210, Jan. 1967, doi: 10.1016/0032-3861(67)90021-3.
[35] M. Bailey and C. Swift, “Input Admittance of a Circular Waveguide Aperture Covered by a Dielectric Slab,” *IEEE Trans. Antennas Propagat.*, vol. 16, no. 4, pp. 386–391, Jul. 1968, doi: 10.1109/TAP.1968.1139207.
[36] G. Smith and J. Nordgard, “Measurement of the electrical constitutive parameters of materials using antennas,” *IEEE Trans. Antennas Propagat.*, vol. 33, no. 7, pp. 783–792, Jul. 1985, doi: 10.1109/TAP.1985.1143657.
[37] S. C. Olson and M. F. Iskander, “A new in situ procedure for measuring the dielectric properties of low permittivity materials,” *IEEE Trans. Instrum. Meas.*, vol. IM–35, no. 1, pp. 2–6, Mar. 1986, doi: 10.1109/TIM.1986.6499047.
[38] M. H. Moussa, M. A. Abu-Khousa, and N. N. Qaddoumi, “Measurement of liquids dielectric property using monopole probes operating at microwave frequencies,” in *10th IEEE International Conference on Electronics, Circuits and Systems, 2003. ICECS 2003. Proceedings of the 2003*, Sharjah, United Arab Emirates, 2003, pp. 1204–1207. doi: 10.1109/ICECS.2003.1301729.
[39] Y. D. He and L. C. Shen, “Measurement of complex permittivity of materials using a monopole antenna,” *IEEE Trans. Geosci. Remote Sensing*, vol. 30, no. 3, pp. 624–627, May 1992, doi: 10.1109/36.142944.
[40] A. Hasan and A. F. Peterson, “Measurement of Complex Permittivity using Artificial Neural Networks,” *IEEE Antennas Propag. Mag.*, vol. 53, no. 1, pp. 200–203, Feb. 2011, doi: 10.1109/MAP.2011.5773614.
[41] S. Roberts and A. Von Hippel, “A New Method for Measuring Dielectric Constant and Loss in the Range of Centimeter Waves,” *Journal of Applied Physics*, vol. 17, no. 7, pp. 610–616, Jul. 1946, doi: 10.1063/1.1707760.
[42] S.-H. Chao, “An uncertainty analysis for the measurement of microwave conductivity and dielectric constant by the short-circuited line method,” *IEEE Trans. Instrum. Meas.*, vol. IM–35, no. 1, pp. 36–41, Mar. 1986, doi: 10.1109/TIM.1986.6499053.
[43] M. A. Saed, S. M. Riad, and W. A. Davis, “Wideband dielectric characterization using a dielectric filled cavity adapted to the end of a transmission line,” *IEEE Trans. Instrum. Meas.*, vol. 39, no. 3, pp. 485–491, Jun. 1990, doi: 10.1109/19.106277.

[44] L. Chen, C. K. Ong, C. P. Neo, V. V. Varadan, and V. K. Varadan, *Microwave electronics: measurement and materials characterisation*. Chichester: John Wiley, 2004.
[45] M. Santra and K. U. Limaye, "Estimation of complex permittivity of arbitrary shape and size dielectric samples using cavity measurement technique at microwave frequencies," *IEEE Trans. Microwave Theory Techn.*, vol. 53, no. 2, pp. 718–722, Feb. 2005, doi: 10.1109/TMTT.2004.840570.
[46] S. Donovan, O. Klein, M. Dressel, K. Holczer, and G. Grüner, "Microwave cavity perturbation technique: Part II: Experimental scheme," *Int J Infrared Milli Waves*, vol. 14, no. 12, pp. 2459–2487, Dec. 1993, doi: 10.1007/BF02086217.
[47] W. Culshaw and M. V. Anderson, "Measurement of Permittivity and Dielectric Loss With a Millimetre-Wave Fabry-Perot Interferometer," *The Proceedings of the IEE - Part B: Electronic and Communication Engineering*, vol. 109, no. 23S, pp. 820–826, 1962.
[48] J. Baker-Jarvis *et al.*, "Dielectric and Magnetic Measurements: A Survey of Nondestructive, Quasi-Nondestructive, and Process-Control Techniques," *Research in Nondestructive Evaluation*, vol. 7, no. 2–3, pp. 117–136, Jan. 1995, doi: 10.1080/09349849509409572.
[49] R. J. Cook, R. G. Jones, and C. B. Rosenberg, "Comparison of Cavity and Open-Resonator Measurements of Permittivity and Loss Angle at 35 GHz," *IEEE Trans. Instrum. Meas.*, vol. 23, no. 4, pp. 438–442, Dec. 1974, doi: 10.1109/TIM.1974.4314330.
[50] S. Chen and M. N. Afsar, "Fabry–Perot Open Resonator Technique for Dielectric Permittivity and Loss Tangent Measurements of Yttrium Iron Garnet," *IEEE Trans. Magn.*, vol. 43, no. 6, pp. 2734–2736, Jun. 2007, doi: 10.1109/TMAG.2007.892855.
[51] B. Komiyama, M. Kiyokawa, and T. Matsui, "Open resonator for precision dielectric measurements in the 100 GHz band," *IEEE Trans. Microwave Theory Techn.*, vol. 39, no. 10, pp. 1792–1796, Oct. 1991, doi: 10.1109/22.88556.
[52] G. Kent, "An evanescent-mode tester for ceramic dielectric substrates," *IEEE Trans. Microwave Theory Techn.*, vol. 36, no. 10, pp. 1451–1454, Oct. 1988, doi: 10.1109/22.6095.
[53] M. D. Janezic, U. Arz, S. Begley, and P. Bartley, "Improved permittivity measurement of dielectric substrates by use of the TE111 mode of a split-cylinder cavity," in *2009 73rd ARFTG Microwave Measurement Conference*, Boston, MA, USA, Jun. 2009, pp. 1–3. doi: 10.1109/ARFTG.2009.5278066.
[54] M. D. Janezic, E. F. Kuester, and J. B. Jarvis, "Broadband complex permittivity measurements of dielectric substrates using a split-cylinder resonator," in *2004 IEEE MTT-S International Microwave Symposium Digest (IEEE Cat. No.04CH37535)*, Fort Worth, TX, USA, 2004, pp. 1817–1820. doi: 10.1109/MWSYM.2004.1338956.
[55] R. Jamal, T. Olivier, P. Damien, D. Nicolas, and V. Serge, "Monitoring of electromagnetic characteristics of split cylinder resonator and dielectric material for temperature caraterization," in *2014 44th European Microwave Conference*, Rome, Oct. 2014, pp. 120–123. doi: 10.1109/EuMC.2014.6986384.
[56] J. Krupka, R. G. Geyer, J. Baker-Jarvis, and J. Ceremuga, "Measurements of the Complex Permittivity of Microwave Circuit Board Substrates Using Split Dielectric Resonator and Reentrant Cavity Techniques," *Seventh International Conference on Dielectric Materials Measurements & Applications*, p. 4, Sep. 1996.
[57] J. Krupka, A. P. Gregory, O. C. Rochard, R. N. Clarke, B. Riddle, and J. Baker-Jarvis, "Uncertainty of complex permittivity measurements by split-post dielectric resonator technique," *Journal of the European Ceramic Society*, vol. 21, no. 15, pp. 2673–2676, Jan. 2001, doi: 10.1016/S0955-2219(01)00343-0.

[58] C. D. Easton, M. V. Jacob, and J. Krupka, “Non-destructive complex permittivity measurement of low permittivity thin film materials,” *Meas. Sci. Technol.*, vol. 18, no. 9, pp. 2869–2877, Sep. 2007, doi: 10.1088/0957-0233/18/9/016.
[59] J. Mazierska, J. Krupka, M. V. Jacob, and D. Ledenyov, “Complex permittivity measurements at variable temperatures of low loss dielectric substrates employing split post and single post dielectric resonators,” in *2004 IEEE MTT-S International Microwave Symposium Digest (IEEE Cat. No.04CH37535)*, Fort Worth, TX, USA, 2004, pp. 1825–1828. doi: 10.1109/MWSYM.2004.1338959.
[60] M. Jacob, J. Krupka, K. Derzakowski, and J. Mazierska, “Mesurements of Thin Polymer Films Employing Split Post Dielectric Resonator Technique,” in *2006 International Conference on Microwaves, Radar & Wireless Communications*, Krakow, Poland, May 2006, pp. 229–231. doi: 10.1109/MIKON.2006.4345156.
[61] R. A. Waldron, “Theory of a Strip-Line Cavity for Measurement of Dielectric Constants and Gyromagnetic-Resonance Line-Widths,” *IEEE Trans. Microwave Theory Techn.*, vol. 12, no. 1, pp. 123–131, Jan. 1964, doi: 10.1109/TMTT.1964.1125760.
[62] P. A. Bernard and J. M. Gautray, “Measurement of dielectric constant using a microstrip ring resonator,” *IEEE Trans. Microwave Theory Techn.*, vol. 39, no. 3, pp. 592–595, Mar. 1991, doi: 10.1109/22.75310.
[63] D. Shimin, “A New Method for Measuring Dielectric Constant Using the Resonant Frequency of a Patch Antenna,” *IEEE Trans. Microwave Theory Techn.*, vol. 34, no. 9, pp. 923–931, Sep. 1986, doi: 10.1109/TMTT.1986.1133472.
[64] Changjun Liu and Yang Pu, “A Microstrip Resonator With Slotted Ground Plane for Complex Permittivity Measurements of Liquids,” *IEEE Microw. Wireless Compon. Lett.*, vol. 18, no. 4, pp. 257–259, Apr. 2008, doi: 10.1109/LMWC.2008.918894.
[65] M. Remsha, M. Manoj, V. A. Shameena, and P. Mohanan, “Complex Permittivity Measurement using Planar Open Stub Resonator,” in *2018 IEEE MTT-S International Microwave and RF Conference (IMaRC)*, Kolkata, India, Nov. 2018, pp. 1–3. doi: 10.1109/IMaRC.2018.8877351.
[66] F. Falcone, T. Lopetegi, J. D. Baena, R. Marques, F. Martin, and M. Sorolla, “Effective negative-ε stopband microstrip lines based on complementary split ring resonators,” *IEEE Microw. Wireless Compon. Lett.*, vol. 14, no. 6, pp. 280–282, Jun. 2004, doi: 10.1109/LMWC.2004.828029.
[67] S. P. Chakyar *et al.*, “Measurement of dielectric constant of waxes at different temperatures using split ring resonator structure,” in *2016 IEEE MTT-S International Microwave and RF Conference (IMaRC)*, New Delhi, Dec. 2016, pp. 1–4. doi: 10.1109/IMaRC.2016.7939638.
[68] A. Ebrahimi, W. Withayachumnankul, S. Al-Sarawi, and D. Abbott, “High-Sensitivity Metamaterial-Inspired Sensor for Microfluidic Dielectric Characterization,” *IEEE Sensors J.*, vol. 14, no. 5, pp. 1345–1351, May 2014, doi: 10.1109/JSEN.2013.2295312.
[69] H.-Y. Gan *et al.*, “Differential Microwave Microfluidic Sensor Based on Microstrip Complementary Split-Ring Resonator (MCSRR) Structure,” *IEEE Sensors J.*, vol. 20, no. 11, pp. 5876–5884, Jun. 2020, doi: 10.1109/JSEN.2020.2973196.
[70] C.-M. Hsu and C.-L. Yang, “High sensitive detection of flow rate and permittivity through microfluidics based on complementary split-ring resonators,” in *2017 IEEE MTT-S International Microwave Symposium (IMS)*, Honolulu, HI, USA, Jun. 2017, pp. 1015–1017. doi: 10.1109/MWSYM.2017.8058762.
[71] A. M. Nicolson and G. F. Ross, “Measurement of the Intrinsic Properties of Materials by Time-Domain Techniques,” *IEEE Trans. Instrum. Meas.*, vol. 19, no. 4, pp. 377–382, Nov. 1970, doi: 10.1109/TIM.1970.4313932.

[72] W. B. Weir, “Automatic measurement of complex dielectric constant and permeability at microwave frequencies,” *Proc. IEEE*, vol. 62, no. 1, pp. 33–36, 1974, doi: 10.1109/PROC.1974.9382.
[73] J. Baker-Jarvis, E. J. Vanzura, and W. A. Kissick, “Improved technique for determining complex permittivity with the transmission/reflection method,” *IEEE Trans. Microwave Theory Techn.*, vol. 38, no. 8, pp. 1096–1103, Aug. 1990, doi: 10.1109/22.57336.
[74] M. Anis, A. Jostingmeier, and A. S. Omar, “Introduction of an effective waveguide width in transmission/reflection methods for dielectric measurements,” in *2007 IEEE Antennas and Propagation Society International Symposium*, Honolulu, HI, Jun. 2007, pp. 281–284. doi: 10.1109/APS.2007.4395485.
[75] F. Ozturk, V. Akan, K. Topalli, E. Kiraz, L. Kuzu, and M. Gokten, “Complex permittivity measurements of dielectrics for space antenna radome and substrates in X-band,” in *2017 International Applied Computational Electromagnetics Society Symposium - Italy (ACES)*, Florence, Mar. 2017, pp. 1–2. doi: 10.23919/ROPACES.2017.7916334.
[76] V. H. Nguyen, M. H. Hoang, H. P. Phan, T. Q. V. Hoang, and T. P. Vuong, “Measurement of complex permittivity by rectangular waveguide method with simple specimen preparation,” in *2014 International Conference on Advanced Technologies for Communications (ATC 2014)*, Hanoi, Vietnam, Oct. 2014, pp. 397–400. doi: 10.1109/ATC.2014.7043419.
[77] J. Hinojosa, “S-parameter broadband measurements on-coplanar and fast extraction of the substrate intrinsic properties,” *IEEE Microw. Wireless Compon. Lett.*, vol. 11, no. 2, pp. 80–82, Feb. 2001, doi: 10.1109/7260.914309.
[78] P. Queffelec, P. Gelin, J. Gieraltowski, and J. Loaec, “A microstrip device for the broad band simultaneous measurement of complex permeability and permittivity,” *IEEE Trans. Magn.*, vol. 30, no. 2, pp. 224–231, Mar. 1994, doi: 10.1109/20.312262.
[79] P. Queffelec, M. Le Floc’h, and P. Gelin, “Broad-band characterization of magnetic and dielectric thin films using a microstrip line,” *IEEE Trans. Instrum. Meas.*, vol. 47, no. 4, pp. 956–963, Aug. 1998, doi: 10.1109/19.744649.
[80] W. Barry, “A Broad-Band, Automated, Stripline Technique for the Simultaneous Measurement of Complex Permittivity and Permeability,” *IEEE Trans. Microwave Theory Techn.*, vol. 34, no. 1, pp. 80–84, Jan. 1986, doi: 10.1109/TMTT.1986.1133283.
[81] E. Salahun, P. Queffelec, M. Le Floc’h, and P. Gelin, “A broadband permeameter for ‘in situ’ measurements of rectangular samples,” *IEEE Trans. Magn.*, vol. 37, no. 4, pp. 2743–2745, Jul. 2001, doi: 10.1109/20.951293.
[82] P. Queffelec, S. Mallegol, and M. LeFloc’h, “Automatic measurement of complex tensorial permeability of magnetized materials in a wide microwave frequency range,” *IEEE Trans. Microwave Theory Techn.*, vol. 50, no. 9, pp. 2128–2134, Sep. 2002, doi: 10.1109/TMTT.2002.802325.
[83] S. S. Stuchly and C. E. Bassey, “Coplanar microwave sensor for industrial measurements,” in *12th International Conference on Microwaves and Radar. MIKON-98. Conference Proceedings (IEEE Cat. No.98EX195)*, Krakow, Poland, 1998, vol. 3, pp. 755–759. doi: 10.1109/MIKON.1998.742821.
[84] Rohde&Schwarz, “Measurement of Dielectric Material Properties.” Apr. 2012.
[85] D. K. Ghodgaonkar, V. V. Varadan, and V. K. Varadan, “A free-space method for measurement of dielectric constants and loss tangents at microwave frequencies,” *IEEE Trans. Instrum. Meas.*, vol. 38, no. 3, pp. 789–793, Jun. 1989, doi: 10.1109/19.32194.
[86] Keysight, “N1501A Dielectric Probe Kit,” *Keysight*. https://www.keysight.com/zz/en/product/N1501A/dielectric-probe-kit.html (accessed Jan. 18, 2022).

[87] SPEAG, Schmid & Partner Engineering AG, “DAK – Dielectric Assessment Kit Product Line.” https://speag.swiss/products/dak/overview/ (accessed Jan. 18, 2022).
[88] APREL, “Dielectric Probe Kit.” https://www.aprel.com/dielectric-probes (accessed Jan. 18, 2022).
[89] KEYCOM Corp., “Probe Mode Open Method Dielectric Constant and Dielectric Loss Tangent Measurement System.” https://keycom.co.jp/eproducts/dps/dps16/page.html (accessed Jan. 18, 2022).
[90] C. Gabriel, “Permittivity Probe Modelling,” Brooks Air Force Base, Texas, USA, Final technical report, Nov. 1991.
[91] J. S. Bobowski and T. Johnson, “Permittivity Measurements of Biological Samples by an Open-Ended Coaxial Line,” *PIER B*, vol. 40, pp. 159–183, 2012, doi: 10.2528/PIERB12022906.
[92] D. Blackham, “Calibration Method for Open-Ended Coaxial Probe/Vector Network Analyzer System,” *MRS Proc.*, vol. 269, p. 595, 1992, doi: 10.1557/PROC-269-595.
[93] K. F. Staebell and D. Misra, “An experimental technique for in vivo permittivity measurement of materials at microwave frequencies,” *IEEE Trans. Microwave Theory Techn.*, vol. 38, no. 3, pp. 337–339, Mar. 1990, doi: 10.1109/22.45358.
[94] S. Bringhurst and M. F. Iskander, “Open-ended metallized ceramic coaxial probe for high-temperature dielectric properties measurements,” *IEEE Trans. Microwave Theory Techn.*, vol. 44, no. 6, pp. 926–935, Jun. 1996, doi: 10.1109/22.506453.
[95] J. Martens, “Open-ended coaxial probe for permittivity measurements to 125 GHz,” *Anritsu*, p. 12, Sep. 2014.
[96] W. Wu and C. E. Smith, “Dielectric measurements using the HP 85070A probe,” in *Proceedings IEEE Southeastcon ’92*, Birmingham, AL, USA, 1992, pp. 83–86. doi: 10.1109/SECON.1992.202313.
[97] A. Fornes-Leal, C. Garcia-Pardo, N. Cardona, S. Sergio Castello-Palacios, and A. Valles-Lluch, “Accurate broadband measurement of electromagnetic tissue phantoms using open-ended coaxial systems,” in *2017 11th International Symposium on Medical Information and Communication Technology (ISMICT)*, Lisbon, Feb. 2017, pp. 32–36. doi: 10.1109/ISMICT.2017.7891761.
[98] N. Wagner, M. Schwing, and A. Scheuermann, “Numerical 3-D FEM and Experimental Analysis of the Open-Ended Coaxial Line Technique for Microwave Dielectric Spectroscopy on Soil,” *IEEE Trans. Geosci. Remote Sensing*, vol. 52, no. 2, pp. 880–893, Feb. 2014, doi: 10.1109/TGRS.2013.2245138.
[99] R. Aminzadeh, M. Saviz, and A. A. Shishegar, “Characterization of low-cost tissue mimicking materials at millimeter-wave frequencies,” in *2015 23rd Iranian Conference on Electrical Engineering*, Tehran, Iran, May 2015, pp. 283–287. doi: 10.1109/IranianCEE.2015.7146225.
[100] G. P. Otto and W. C. Chew, “Improved calibration of a large open-ended coaxial probe for dielectric measurements,” *IEEE Trans. Instrum. Meas.*, vol. 40, no. 4, pp. 742–746, Aug. 1991, doi: 10.1109/19.85345.
[101] H. Zheng and C. E. Smith, “Permittivity measurements using a short open-ended coaxial line probe,” *IEEE Microw. Guid. Wave Lett.*, vol. 1, no. 11, pp. 337–339, Nov. 1991, doi: 10.1109/75.93904.
[102] P. De Langhe, L. Martens, and D. De Zutter, “Design rules for an experimental setup using an open-ended coaxial probe based on theoretical modelling,” *IEEE Trans. Instrum. Meas.*, vol. 43, no. 6, pp. 810–817, Dec. 1994, doi: 10.1109/19.368062.
[103] M. Okoniewski, J. Anderson, E. Okoniewska, K. Caputa, and S. S. Stuchly, “Further analysis of open-ended dielectric sensors,” *IEEE Trans. Microwave Theory Techn.*, vol. 43, no. 8, pp. 1986–1989, Aug. 1995, doi: 10.1109/22.402291.

[104] A. Fallahi, S. Hashemizadeh, and N. Kuster, “On the Dielectric Measurement of Thin Layers Using Open-Ended Coaxial Probes,” *IEEE Trans. Instrum. Meas.*, vol. 70, pp. 1–8, 2021, doi: 10.1109/TIM.2021.3123257.
[105] D. Berube, F. M. Ghannouchi, and P. Savard, “A comparative study of four open-ended coaxial probe models for permittivity measurements of lossy dielectric/biological materials at microwave frequencies,” *IEEE Trans. Microwave Theory Techn.*, vol. 44, no. 10, pp. 1928–1934, Oct. 1996, doi: 10.1109/22.539951.
[106] T. W. Athey, M. A. Stuchly, and S. S. Stuchly, “Measurement of Radio Frequency Permittivity of Biological Tissues with an Open-Ended Coaxial Line: Part I,” *IEEE Transactions on Microwave Theory and Techniques*, vol. 30, no. 1, pp. 82–86, Jan. 1982, doi: 10.1109/TMTT.1982.1131021.
[107] W. J. Ellison and J.-M. Moreau, “Open-Ended Coaxial Probe: Model Limitations,” *IEEE Trans. Instrum. Meas.*, vol. 57, no. 9, pp. 1984–1991, Sep. 2008, doi: 10.1109/TIM.2008.917683.
[108] G. Ruvio, M. Vaselli, V. Lopresto, R. Pinto, L. Farina, and M. Cavagnaro, “Comparison of different methods for dielectric properties measurements in liquid sample media,” *Int J RF Microw Comput Aided Eng*, vol. 28, no. 3, p. e21215, Mar. 2018, doi: 10.1002/mmce.21215.
[109] T. J. Yoon *et al.*, “Dielectric relaxation of neodymium chloride in water and in methanol,” *Journal of Molecular Liquids*, vol. 308, p. 112981, Jun. 2020, doi: 10.1016/j.molliq.2020.112981.
[110] J. Wang, E. G. Lim, M. P. Leach, Z. Wang, and K. L. Man, “Open-Ended Coaxial Cable Selection for Measurement of Liquid Dielectric Properties via the Reflection Method,” *Mathematical Problems in Engineering*, vol. 2020, pp. 1–8, Oct. 2020, doi: 10.1155/2020/8942096.
[111] M. M. Brady, S. A. Symons, and S. S. Stuchly, “Dielectric Behavior of Selected Animal Tissues in Vitro at Frequencies from 2 to 4 GHz,” *IEEE Trans. Biomed. Eng.*, vol. BME-28, no. 3, pp. 305–307, Mar. 1981, doi: 10.1109/TBME.1981.324707.
[112] C. L. Sibbald, “A new technique for modelling open-ended waveguide structures and its application to dielectric spectroscopy.,” Ottawa-Carleton Institute for Electrical Engineering, University of Ottawa, Canada, 1992.
[113] J. M. Anderson, C. L. Sibbald, S. S. Stuchly, and K. Caputa, “Advances in dielectric measurements using an open-ended coaxial line sensor,” in *Proceedings of Canadian Conference on Electrical and Computer Engineering*, Vancouver, BC, Canada, 1993, pp. 916–919. doi: 10.1109/CCECE.1993.332443.
[114] J. M. Anderson, C. L. Sibbald, and S. S. Stuchly, “Dielectric measurements using a rational function model,” *IEEE Trans. Microwave Theory Techn.*, vol. 42, no. 2, pp. 199–204, Feb. 1994, doi: 10.1109/22.275247.
[115] F. M. Ghannouchi and R. G. Bosisio, “Measurement of microwave permittivity using a six-port reflectometer with an open-ended coaxial line,” *IEEE Trans. Instrum. Meas.*, vol. 38, no. 2, pp. 505–508, Apr. 1989, doi: 10.1109/19.192335.
[116] M. Ragulskis *et al.*, “Effect of Network Analyzer Trace Noise on Dielectric Measurements with an Open-ended Coaxial Probe,” in *12th European Conference on Antennas and Propagation (EuCAP 2018)*, London, UK, 2018, p. 570 (5 pp.)-570 (5 pp.). doi: 10.1049/cp.2018.0929.
[117] Y. Feldman, E. Polygalov, I. Ermolina, Y. Polevaya, and B. Tsentsiper, “Electrode polarization correction in time domain dielectric spectroscopy,” *Meas. Sci. Technol.*, vol. 12, no. 8, pp. 1355–1364, Aug. 2001, doi: 10.1088/0957-0233/12/8/351.
[118] P. B. Ishai, Z. Sobol, J. D. Nickels, A. L. Agapov, and A. P. Sokolov, “An assessment of comparative methods for approaching electrode polarization in dielectric

permittivity measurements,” *Review of Scientific Instruments*, vol. 83, no. 8, p. 083118, Aug. 2012, doi: 10.1063/1.4746992.
[119] M. A. Maury, “Microwave Coaxial Connector Technology: A Continuing Evolution,” p. 21, 2005.
[120] Amphenol RF Connex, “SMA Coaxial Connectors Datasheet.” 2011.
[121] Maury Microwave Corporation, “Precision 3.5mm (APC3.5) Coaxial Connectors.” Mar. 2013.
[122] Maury Microwave Corporation, “Precision 2.4mm (GPC2.4) Coaxial Connectors.” Oct. 1997.
[123] T. P. Marsland and S. Evans, “Dielectric measurements with an open-ended coaxial probe,” *IEE Proc. H Microw. Antennas Propag. UK*, vol. 134, no. 4, p. 341, 1987, doi: 10.1049/ip-h-2.1987.0068.
[124] K. Shibata and M. Kobayashi, “Property Measurement Errors Based on Application of an Estimation Equation Using the Coaxial Probe Method,” in *2019 IEEE MTT-S International Microwave and RF Conference (IMARC)*, Mumbai, India, Dec. 2019, pp. 1–5. doi: 10.1109/IMaRC45935.2019.9118702.
[125] V. Guihard, F. Taillade, J.-P. Balayssac, B. Steck, J. Sanahuja, and F. Deby, “Modelling the behaviour of an open-ended coaxial probe to assess the permittivity of heterogeneous dielectrics solids,” in *2017 Progress In Electromagnetics Research Symposium - Spring (PIERS)*, St. Petersburg, May 2017, pp. 1650–1656. doi: 10.1109/PIERS.2017.8262014.
[126] S. O. Nelson and P. G. Bartley, “Open-ended coaxial probe permittivity measurements on pulverized materials,” in *IEEE Instrumentation and Measurement Technology Conference Sensing, Processing, Networking. IMTC Proceedings*, Ottawa, Ont., Canada, 1997, vol. 1, pp. 653–657. doi: 10.1109/IMTC.1997.604033.
[127] D. A. G. Bruggeman, “Berechnung verschiedener physikalischer Konstanten von heterogenen Substanzen. I. Dielektrizitätskonstanten und Leitfähigkeiten der Mischkörper aus isotropen Substanzen,” *Ann. Phys.*, vol. 416, no. 7, pp. 636–664, 1935, doi: 10.1002/andp.19354160705.
[128] J. C. Maxwell Garnett, “Colours in Metal Glasses and in Metallic Films,” *Philosophical Transactions of the Royal Society*, vol. A, no. 203, pp. 385–420, 1904.
[129] E. Baharudin *et al.*, “Determination of pulverized material permittivity for microwave absorber application,” in *RSM 2013 IEEE Regional Symposium on Micro and Nanoelectronics*, Daerah Langkawi, Malaysia, Sep. 2013, pp. 85–88. doi: 10.1109/RSM.2013.6706479.
[130] E. Odelstad, S. Raman, A. Rydberg, and R. Augustine, “Experimental Procedure for Determination of the Dielectric Properties of Biological Samples in the 2-50 GHz Range,” *IEEE J. Transl. Eng. Health Med.*, vol. 2, pp. 1–8, 2014, doi: 10.1109/JTEHM.2014.2340412.
[131] G. Chen, Kang Li, and Zhong Ji, “Bilayered dielectric measurement with an open-ended coaxial probe,” *IEEE Trans. Microwave Theory Techn.*, vol. 42, no. 6, pp. 966–971, Jun. 1994, doi: 10.1109/22.293564.
[132] C.-L. Li and K.-M. Chen, “Determination of electromagnetic properties of materials using flanged open-ended coaxial probe-full-wave analysis,” *IEEE Trans. Instrum. Meas.*, vol. 44, no. 1, pp. 19–27, Feb. 1995, doi: 10.1109/19.368108.
[133] C. Aydinalp, S. Joof, I. Akduman, and T. Yilmaz, “Sensitivity and Sensing Depth Analysis of Open-ended Contact Probes for Cancer Diagnosis,” in *2019 PhotonIcs & Electromagnetics Research Symposium - Spring (PIERS-Spring)*, Rome, Italy, Jun. 2019, pp. 2523–2528. doi: 10.1109/PIERS-Spring46901.2019.9017401.

[134] E. Porter, A. L. Gioia, A. Santorelli, and M. O'Halloran, "Modeling of the dielectric properties of biological tissues within the histology region," *IEEE Trans. Dielect. Electr. Insul.*, vol. 24, no. 5, pp. 3290–3301, Oct. 2017, doi: 10.1109/TDEI.2017.006690.
[135] A. La Gioia, E. Porter, S. Salahuddin, and M. O'Halloran, "Impact of Radial Heterogeneities of Biological Tissues on Dielectric Measurements," in *2017 International Conference on Electromagnetics in Advanced Applications (ICEAA)*, Verona, Sep. 2017, pp. 421–424. doi: 10.1109/ICEAA.2017.8065267.
[136] P. M. Meaney, A. P. Gregory, N. R. Epstein, and K. D. Paulsen, "Microwave open-ended coaxial dielectric probe: interpretation of the sensing volume re-visited," *BMC Med Phys*, vol. 14, no. 1, p. 3, Dec. 2014, doi: 10.1186/1756-6649-14-3.
[137] P. M. Meaney, A. P. Gregory, J. Seppala, and T. Lahtinen, "Open-Ended Coaxial Dielectric Probe Effective Penetration Depth Determination," *IEEE Trans. Microwave Theory Techn.*, pp. 1–9, 2016, doi: 10.1109/TMTT.2016.2519027.
[138] A. Šarolić, "Open-Ended Coaxial Dielectric Probe Model for Biological Tissue Sensing Depth Analysis at 2 GHz," in *2019 European Microwave Conference in Central Europe (EuMCE)*, May 2019, pp. 605–608.
[139] A. Šarolić and A. Matković, "Effect of the Coaxial Dielectric Probe Diameter on Its Permittivity Sensing Depth at 2 GHz – Simulation Study.," in *Proceedings of 23rd International Conference on Applied Electromagnetics and Communications - ICECOM 2019*, Dubrovnik, Croatia, 2019, p. 4.
[140] J. Baker-Jarvis, M. D. Janezic, P. D. Domich, and R. G. Geyer, "Analysis of an open-ended coaxial probe with lift-off for nondestructive testing," *IEEE Trans. Instrum. Meas.*, vol. 43, no. 5, pp. 711–718, Oct. 1994, doi: 10.1109/19.328897.
[141] H. C. Reader and M. D. Janezic, "Coaxial probe dielectric measurements: Practical dotting 'i's' and crossing 't's,'" in *2006 68th ARFTG Conference: Microwave Measurement*, Broomfield, CO, USA, Nov. 2006, pp. 1–7. doi: 10.1109/ARFTG.2006.8361673.
[142] S. Bringhurst and M. F. Iskander, "FDTD analysis of dielectric properties measurements using open-ended coaxial probes," in *IEEE Antennas and Propagation Society International Symposium. 1996 Digest*, Baltimore, MD, USA, 1996, vol. 2, pp. 1032–1035. doi: 10.1109/APS.1996.549772.
[143] S. Bringhurst, M. F. Iskander, and M. J. White, "Thin-sample measurements and error analysis of high-temperature coaxial dielectric probes," *IEEE Trans. Microwave Theory Techn.*, vol. 45, no. 12, pp. 2073–2083, Dec. 1997, doi: 10.1109/22.643740.
[144] K. C. McDonald, R. Zimmermann, J. Way, and W. Chun, "Automated instrumentation for continuous monitoring of the dielectric properties of woody vegetation: system design, implementation, and selected in situ measurements," *IEEE Trans. Geosci. Remote Sensing*, vol. 37, no. 4, pp. 1880–1894, Jul. 1999, doi: 10.1109/36.774701.
[145] E. C. Burdette, F. L. Cain, and J. Seals, "In Vivo Probe Measurement Technique for Determining Dielectric Properties at VHF through Microwave Frequencies," *IEEE Trans. Microwave Theory Techn.*, vol. 28, no. 4, pp. 414–427, Apr. 1980, doi: 10.1109/TMTT.1980.1130087.
[146] A. Peyman, C. Gabriel, E. H. Grant, G. Vermeeren, and L. Martens, "Variation of the dielectric properties of tissues with age: the effect on the values of SAR in children when exposed to walkie–talkie devices," *Phys. Med. Biol.*, vol. 54, no. 2, pp. 227–241, Jan. 2009, doi: 10.1088/0031-9155/54/2/004.
[147] K. Chand, P. Mehta, D. G. Beetner, R. Zoughi, and W. V. Stoecker, "Microwave Reflectometry as a Novel Diagnostic Method for Detection of Skin Cancers," in *2005*

IEEE Instrumentationand Measurement Technology Conference Proceedings, Ottawa, ON, Canada, 2005, vol. 2, pp. 1425–1428. doi: 10.1109/IMTC.2005.1604385.
[148] B. L. Shrestha, H. C. Wood, and S. Sokhansanj, "Microwave Dielectric Properties of Alfalfa Leaves From 0.3 to 18 GHz," *IEEE Trans. Instrum. Meas.*, vol. 60, no. 8, pp. 2926–2933, Aug. 2011, doi: 10.1109/TIM.2011.2121270.
[149] M. El-rayes and F. Ulaby, "Microwave Dielectric Spectrum of Vegetation-Part I: Experimental Observations," *IEEE Trans. Geosci. Remote Sensing*, vol. GE-25, no. 5, pp. 541–549, Sep. 1987, doi: 10.1109/TGRS.1987.289832.
[150] A. Martellosio *et al.*, "Dielectric Properties Characterization From 0.5 to 50 GHz of Breast Cancer Tissues," *IEEE Trans. Microwave Theory Techn.*, vol. 65, no. 3, pp. 998–1011, Mar. 2017, doi: 10.1109/TMTT.2016.2631162.
[151] S. A. R. Naqvi, M. Manoufali, B. Mohammed, A. T. Mobashsher, D. Foong, and A. M. Abbosh, "In Vivo Human Skin Dielectric Properties Characterization and Statistical Analysis at Frequencies From 1 to 30 GHz," *IEEE Trans. Instrum. Meas.*, vol. 70, pp. 1–10, 2021, doi: 10.1109/TIM.2020.3036767.
[152] P. Mehta, K. Chand, D. Narayanswamy, D. G. Beetner, R. Zoughi, and W. V. Stoecker, "Microwave Reflectometry as a Novel Diagnostic Tool for Detection of Skin Cancers," *IEEE Trans. Instrum. Meas.*, vol. 55, no. 4, pp. 1309–1316, Aug. 2006, doi: 10.1109/TIM.2006.876566.
[153] G. Maenhout, T. Markovic, I. Ocket, and B. Nauwelaers, "Effect of Open-Ended Coaxial Probe-to-Tissue Contact Pressure on Dielectric Measurements," *Sensors*, vol. 20, no. 7, p. 2060, Apr. 2020, doi: 10.3390/s20072060.
[154] S. K. Lau, D. Dag, S. Ozturk, F. Kong, and J. Subbiah, "A comparison between the open-ended coaxial probe method and the parallel plate method for measuring the dielectric properties of low-moisture foods," *LWT*, vol. 130, p. 109719, Aug. 2020, doi: 10.1016/j.lwt.2020.109719.
[155] J. C. A. Santos, M. H. C. Dias, A. P. Aguiar, I. B. Jr, and L. E. P. Borges, "Using the Coaxial Probe Method for Permittivity Measurements of Liquids at High Temperatures," vol. 8, no. 1, p. 14, 2009.
[156] D. M. Hagl, D. Popovic, S. C. Hagness, J. H. Booske, and M. Okoniewski, "Sensing volume of open-ended coaxial probes for dielectric characterization of breast tissue at microwave frequencies," *IEEE Trans. Microwave Theory Techn.*, vol. 51, no. 4, pp. 1194–1206, Apr. 2003, doi: 10.1109/TMTT.2003.809626.
[157] A. La Gioia, E. Porter, and M. O'Halloran, "Examination of the sensing radius of open-ended coaxial probes in dielectric measurements of biological tissues," in *2017 IEEE International Symposium on Antennas and Propagation & USNC/URSI National Radio Science Meeting*, San Diego, CA, USA, Jul. 2017, pp. 215–216. doi: 10.1109/APUSNCURSINRSM.2017.8072150.
[158] A. La Gioia, M. O'Halloran, and E. Porter, "Modelling the Sensing Radius of a Coaxial Probe for Dielectric Characterisation of Biological Tissues," *IEEE Access*, vol. 6, pp. 46516–46526, 2018, doi: 10.1109/ACCESS.2018.2866703.
[159] A. La Gioia, M. O'Halloran, A. Elahi, and E. Porter, "Investigation of histology radius for dielectric characterisation of heterogeneous materials," *IEEE Trans. Dielect. Electr. Insul.*, vol. 25, no. 3, pp. 1064–1079, Jun. 2018, doi: 10.1109/TDEI.2018.006912.
[160] A. La Gioia, S. Salahuddin, M. O'Halloran, and E. Porter, "Quantification of the Sensing Radius of a Coaxial Probe for Accurate Interpretation of Heterogeneous Tissue Dielectric Data," *IEEE J. Electromagn. RF Microw. Med. Biol.*, vol. 2, no. 3, pp. 145–153, Sep. 2018, doi: 10.1109/JERM.2018.2841798.
[161] A. La Gioia, M. O'Halloran, and E. Porter, "Modelling of Tissue Dielectric Contribution Within the Sensing Radius of a Coaxial Probe," in *2018 EMF-Med 1st*

World Conference on Biomedical Applications of Electromagnetic Fields (EMF-Med), Split, Sep. 2018, pp. 1–2. doi: 10.23919/EMF-MED.2018.8526046.
[162] A. La Gioia, M. O'Halloran, and E. Porter, "Sensing Radius of an Open-Ended Coaxial Probe for Dielectric Measurement of Tissues: Calculation with Relative Permittivity versus Conductivity," in *2019 URSI Asia-Pacific Radio Science Conference (AP-RASC)*, New Delhi, India, Mar. 2019, pp. 1–4. doi: 10.23919/URSIAP-RASC.2019.8738385.
[163] A. La Gioia, A. Santorelli, M. O'Halloran, and E. Porter, "Predicting the Sensing Radius of a Coaxial Probe Based on the Probe Dimensions," *IEEE Trans. Antennas Propagat.*, vol. 68, no. 9, pp. 6704–6716, Sep. 2020, doi: 10.1109/TAP.2020.2986708.
[164] A. Farshkaran and E. Porter, "Improved Sensing Volume Estimates for Coaxial Probes to Measure the Dielectric Properties of Inhomogeneous Tissues," *IEEE J. Electromagn. RF Microw. Med. Biol.*, pp. 1–7, 2022, doi: 10.1109/JERM.2021.3133076.

Abbreviation list

CRIM	complex refractive index model
CSRR	complementary split ring resonator
EMF	electromagnetic field
EP	electrode polarization
FEM	finite element method
FDTD	finite-difference time-domain
LRL	line-reflect-line
MoM	method of moments
MUT	material under test
OECP	open-ended coaxial probe
PEC	perfect electric conductor
SRR	split ring resonator
TE	transverse electric
TEM	transverse electromagnetic
TM	transverse magnetic
TL	transmission line
TRL	through-reflect-line
TRM	through-reflect-match
VNA	vector network analyzer

Abstract

Complex dielectric permittivity is an important electromagnetic property of a material, usable in diverse applications. Essentially it describes the material response to the electric field, however, indirectly it can also uncover differences in the state of the material, as the permittivity varies with temperature, moisture content, pH value, pressure, and other physical quantities. It can therefore be used for various purposes: from monitoring the quality of food through determining soil compositions and all the way to monitoring the state of biological tissues. Consequently, over the last several decades the number of dielectric measurement methods and their variations kept growing. Given that each method has its advantages and disadvantages, depending on the material measured and the measurement setup, some methods are more suitable than others. This work provides an overview of dielectric measurement methods used in the microwave range. Since there is a fair number of methods presented, the methods are divided into three groups: reflection methods, resonance methods and reflection/transmission methods. After the detailed review of the methods, further focus is only on the open-ended coaxial probe. First, a theoretical foundation based on microwave measurements is given, followed by various analytical methods that allow for calculation of the complex dielectric permittivity from the complex reflection coefficient measured by a vector network analyzer. Subsequently, a detailed explanation of the calibration of a coaxial probe is given as it removes systematic errors from the measurements and ensures adequate results of the measured complex permittivity. The last chapter is dedicated to the currently unresolved limitations of this method that prevent its even wider application. First, the frequency limitations of the probe are covered and general explanations of the reasons for the existence of the upper and lower limit frequencies are given. Incomplete contact of the probe and the sample resulting in air pockets between the probe and the sample also introduces measurement errors that are not easy to define and eliminate. Finally, the general problem of determining the sensing volume of the coaxial probe is also addressed. Without the exact understanding of the sensing volume (i.e. the sensing depth and radius), it is difficult to accurately characterize a sample being either too small or exhibiting any of the various types of inhomogeneities, which is discussed in depth in the last chapter.

Keywords: complex dielectric permittivity of materials; dielectric measurements in microwave range; reflection, resonant and transmission/reflection measurement methods; open-ended coaxial probe method using vector network analyzer (VNA); calibration scattering matrix, equivalent circuits and de-embedding models

Sažetak

Kompleksna dielektrična permitivnost je važno elektromagnetsko svojstvo materijala koje se može koristiti u različitim primjenama. Iako opisuje ponašanje materijala u električnom polju, posredno može otkriti i razlike u stanju materijala budući da varira s temperaturom, vlažnosti, pH vrijednosti, tlakom i drugim fizičkim veličinama. Stoga se može koristiti u različite svrhe: od kontroliranja kvalitete hrane preko određivanja sastava tla pa sve do praćenja stanja bioloških tkiva. Posljedično, tijekom posljednjih nekoliko desetljeća broj metoda mjerenja dielektrične permitivnosti kontinuirano raste. S obzirom na to da svaka metoda ima svoje prednosti i nedostatke, ovisno o mjernom materijalu i postavu, neke metode su prikladnije od drugih. Ovaj rad daje pregled mjernih metoda dielektrične permitivnosti koje se koriste u mikrovalnom rasponu. Budući da ima dosta različitih opisanih metoda, metode su podijeljene u tri grupe: metode refleksije, metode rezonancije i metode transmisije/refleksije. Nakon detaljnog pregleda metoda, daljnji fokus je samo na koaksijalnoj sondi otvorenog kraja. Najprije se daje teorijska osnova temeljena na mikrovalnim mjerenjima, a zatim slijede različite analitičke metode koje omogućuju izračun kompleksne dielektrične permitivnosti iz kompleksnog refleksijskog koeficijenta koeficijenta izmjerenog na vektorskom analizatoru mreža. Potom se daje detaljno objašnjenje kalibracije koaksijalne sonde koja uklanja sustavne pogreške iz mjerenja i osigurava adekvatne rezultate izmjerene kompleksne dielektrične permitivnosti. Posljednje poglavlje posvećeno je aktualnim neriješenim ograničenjima ove metode koja sprječavaju njezinu širu primjenu. Najprije se obrađuju frekvencijska ograničenja sonde i daju opća objašnjenja razloga postojanja gornje i donje granične frekvencije. Nepotpuni kontakt sonde i uzorka rezultira džepovima zraka između sonde i uzorka što također unosi pogreške u mjerenja koje nije lako definirati i eliminirati. Konačno, obrađen je i opći problem određivanja mjernog volumena sonde. Bez točnog razumijevanja mjernog volumena (tj. dubine i radijusa mjerenja), teško je točno odrediti je li uzorak premalen ili je li pokazuje bilo koju od različitih vrsta nehomogenosti, o čemu se detaljno raspravlja u posljednjem poglavlju.

Ključne riječi: kompleksna dielektrična permitivnost materijala; dielektrična mjerenja u mikrovalnom području; mjerne metode refleksije, rezonancije i transmisije/refleksije; mjerenje koaksijalnom sondom otvorenog kraja pomoću vektorskog analizatora mreža (VNA); matrica raspršnih parametara kalibracije, nadomjesni sklopovi i modeli proračuna dielektrične permitivnosti